ADVANCED BIOLOGY
www.advanced-bio.com

3D Bioprinted Neural-Like Tissue as a Platform to Study Neurotropism of Mouse-Adapted SARS-CoV-2

Bruna A. G. de Melo, Mayara V. Mundim, Robertha M. R. Lemes, Elisa M. Cruz, Tais N. Ribeiro, Carolina F. Santiago, Jéssica H. L. da Fonsêca, Julia C. Benincasa, Roberta S. Stilhano, Nathalia Mantovani, Luiz C. Santana, Ricardo Durães-Carvalho, Ricardo S. Diaz, Luiz M. R. Janini, Juliana T. Maricato, and Marimelia A. Porcionatto**

The effects of neuroinvasion by severe acute respiratory syndrome coronavirus 2 (SARS-CoV-2) become clinically relevant due to the numerous neurological symptoms observed in Corona Virus Disease 2019 (COVID-19) patients during infection and post-COVID syndrome or long COVID. This study reports the biofabrication of a 3D bioprinted neural-like tissue as a proof-of-concept platform for a more representative study of SARS-CoV-2 brain infection. Bioink is optimized regarding its biophysical properties and is mixed with murine neural cells to construct a 3D model of COVID-19 infection. Aiming to increase the specificity to murine cells, SARS-CoV-2 is mouse-adapted (MA-SARS-CoV-2) in vitro, in a protocol first reported here. MA-SARS-CoV-2 reveals mutations located at the Orf1a and Orf3a domains and is evolutionarily closer to the original Wuhan SARS-CoV-2 strain than SARS-CoV-2 used for adaptation. Remarkably, MA-SARS-CoV-2 shows high specificity to murine cells, which present distinct responses when cultured in 2D and 3D systems, regarding cell morphology, neuroinflammation, and virus titration. MA-SARS-CoV-2 represents a valuable tool in studies using animal models, and the 3D neural-like tissue serves as a powerful in vitro platform for modeling brain infection, contributing to the development of antivirals and new treatments for COVID-19.

1. Introduction

The Corona Virus Disease 2019 (COVID-19) pandemic emerged in December 2019,[1] and the research community still faces several challenges regarding the development and testing of vaccines and antivirals against the severe acute respiratory syndrome coronavirus 2 (SARS-CoV-2). Although the global scientific and medical community achieved significant advances in vaccines and treatment,[2] the virus continues to spread, and many countries face new waves of the pandemic, with over 6 million confirmed deaths as of April 2022.[3]

The respiratory tract is the first target of SARS-CoV-2, and much evidence revealed the capacity of the virus to spread and infect other human organs expressing the angiotensin-converting enzyme 2 (ACE2), the primary receptor for SARS-CoV-2,[4] such as the liver,[5] the gastrointestinal

B. A. G. Melo, M. V. Mundim, E. M. Cruz, T. N. Ribeiro, J. C. Benincasa, M. A. Porcionatto
Department of Biochemistry
Escola Paulista de Medicina
Universidade Federal de São Paulo
São Paulo 04039-032, Brazil
E-mail: marimelia.porcionatto@unifesp.br

R. M. R. Lemes
Department of Biological Sciences
Universidade Federal de São Paulo
Diadema 09920-540, Brazil

C. F. Santiago, R. Durães-Carvalho, L. M. R. Janini, J. T. Maricato
Department of Microbiology
Immunology and Parasitoloy
Escola Paulista de Medicina
Universidade Federal de São Paulo
São Paulo 04039-032, Brazil
E-mail: juliana.maricato@unifesp.br

J. H. L. da Fonsêca
Department of Manufacturing and Materials Engineering
Faculdade de Engenharia Mecânica
Universidade Estadual de Campinas
Campinas, SP 13083-860, Brazil

R. S. Stilhano
Department of Physiological Sciences
Faculdade de Ciências Médicas
Santa Casa de São Paulo
São Paulo 01221-020, Brazil

N. Mantovani, L. C. Santana, R. S. Diaz
Department of Medicine
Escola Paulista de Medicina
Universidade Federal de São Paulo
São Paulo 04039-032, Brazil

The ORCID identification number(s) for the author(s) of this article can be found under https://doi.org/10.1002/adbi.202200002.

DOI: 10.1002/adbi.202200002

tract,[6] the heart,[7] and the central nervous system (CNS).[8] Clinical reports of patients infected with SARS-CoV-2 evidenced neurological manifestations, such as cerebrovascular events, ischemic stroke, intracerebral hemorrhage, and altered mental status.[9] Furthermore, the long-term effects of the disease in the brain and neurological sequelae are particularly worrying. Thus, the investigation of SARS-CoV-2 neurotropism is of high interest.

3D in vitro models are helpful to characterize the pathogenesis of the virus in a complex organ such as the brain, in addition to validating therapeutics prior to clinical trials. Organoids, assembloids, and spheroids have been used to study the effects of SARS-CoV-2 infection in the CNS.[10–14] However, these structures lack reproducibility due to spontaneous and uncontrolled cellular aggregation. On the other hand, biofabrication techniques, such as 3D bioprinting, provide a more organized, controlled, and reproducible construction of tissue-like structures, highly relevant for studying viruses' infection in multiple organs and tissues.[15–17] Through a spatial and precise distribution of cells and biomaterials, the extrusion-based 3D bioprinting technique allows the construction of structures that better mimic the complexity of the CNS microenvironment regarding cell-cell and cell-matrix interactions, as well as the natural patterns of infection.[17,18]

The brain is one of the softest tissues of the human body,[19] making the development of bioinks to bioprint brain-like structures challenging. It requires the combination of biomaterials and extracellular matrix (ECM) proteins that allow extrusion and maintenance of the 3D construct while contributing to high viability and functionality of neural cells. The bioink described here is composed of gelatin methacryloyl (GelMA), fibrin, and laminin and showed tunable biophysical properties suitable for bioprinting and culture of neural cells derived from C57Bl/6 mice.

Murine cells and animal models provide a wealth of information about the effects of several viruses in the brain,[20] including SARS-CoV-2 infectivity.[21–23] However, due to the low affinity of SARS-CoV-2 to mouse ACE2, mice models are less susceptible to the human strain infection,[24] which has led to the use of transgenic mice expressing human ACE2.[25–27] Nevertheless, SARS-CoV-2 mouse-adaptation is an alternative to assure the infection and replication in small, low cost, and well-established animal models,[24,28,29] as well as in vitro models fabricated using murine cells, besides preventing lethality and distinct tropism that SARS-CoV-2 infection may cause in transgenic models.[30–33] This approach also enables the use of genetic knockout mice,[34] widening the range of studies involving the mechanisms of infection.

In this work, we report the in vitro generation of a mouse-adapted strain of SARS-CoV-2 (MA-SARS-CoV-2), after four passages of the human strain (hSARS-CoV-2), through a more straightforward protocol compared to protocols of in vivo virus adaptation, aiming the infection of the 3D neural-like tissue. The bioprinted model, biofabricated using murine cells and brain-featured bioink, represents a proof-of-concept platform for SARS-CoV-2 infection, being a valuable tool to understand the pathological effects of COVID-19 in the CNS.

2. Results and Discussion

2.1. Development and Optimization of Bioinks

To mimic the intricacy of the neural tissue, the mechanical and physical properties of the bioink must be optimized, as well as its bioprintability and rheology, crucial properties to allow the 3D bioprinting process. A combination of gelatin, GelMA, and fibrinogen, supplemented (GGFL) or not (GGF) with laminin, was used as the bioink composition for 3D extrusion, forming a hydrogel in a two-step crosslinking process (**Figure 1**A). GGF was composed of 5% (w/v) gelatin, 5% (w/v) GelMA, and 1.5 mg mL^{-1} fibrinogen, while GGFL of 4% (w/v) gelatin, 2% (w/v) GelMA, 3 mg mL^{-1} fibrinogen, and 2 µg mL^{-1} laminin. Both compositions were tested in order to determine an optimized concentration of gelatin, to assure the bioink's printability, GelMA, and fibrinogen, to assure mechanical and physical stability, and laminin, to stimulate cells' biological behavior.

The presence of gelatin directly influences the bioink's rheology and assures the printability of the composition when using an extrusion bioprinting method, due to its viscoelasticity and sol-gel transition capacity.[16,35] GGF and GGFL bioinks showed distinct sol-gel transition range, evaluated in terms of loss (G'') and storage (G') moduli variation (Figure 1B). While transition of GGF was within the range of 25 °C to 19 °C, GGFL required lower temperature for the sol-gel transition during bioprinting, with this range being between 22 °C to 15 °C. GGF showed increased viscosity variation with shear rate as compared to GGFL (Figure 1C) and presented higher flow consistency index (K) (2.529 and 1.853, respectively) and lower power law index (n) (0.505 and 0.596, respectively) (Table S1, Supporting Information), calculated from the shear stress versus shear rate curves (Figure S1, Supporting Information). These results indicate a superior shear-thinning behavior of GGF, although both, GGF and GGFL, showed to be pseudoplastic fluids with non-Newtonian behavior, which is favorable for extrusion and maintenance of the 3D structure.[36] Furthermore, frequency sweep (0.1 to 300 rad s^{-1}) showed that the elasticity of both compositions was superior to viscosity ($G' > G''$), emphasizing their gel-like behavior (Figure 1D).

After crosslinking and hydrogel's incubation at 37 °C, GelMA and fibrin fibers formed interpenetrated polymer networks (IPNs), while gelatin was gradually diffused from the structure. Hydrogels' physical stability was assessed by hydrolytic degradation, showing that mass loss increased exponentially in the first 8 h, due to the diffusion of non-crosslinked gelatin (Figure 1E). Then, degradation continued to increase gradually up to 7 d, stabilizing within 2 weeks, being significantly higher for GGFL as compared to GGF, probably due to the lower concentration of GelMA in the composition. However, both hydrogels were considered stable for cell culture.

The brain is one of the softest tissues in the human body, with mechanical modulus of 0.1–3 kPa.[19,37] This is a crucial feature to be mimicked, as matrix stiffness plays a key role in directing neural cells behavior,[38] with several previous works reporting that matrix stiffness <10 kPa provides a more favorable microenvironment to preserve neural cells' functionality.[39–41] Mechanical properties were assessed by

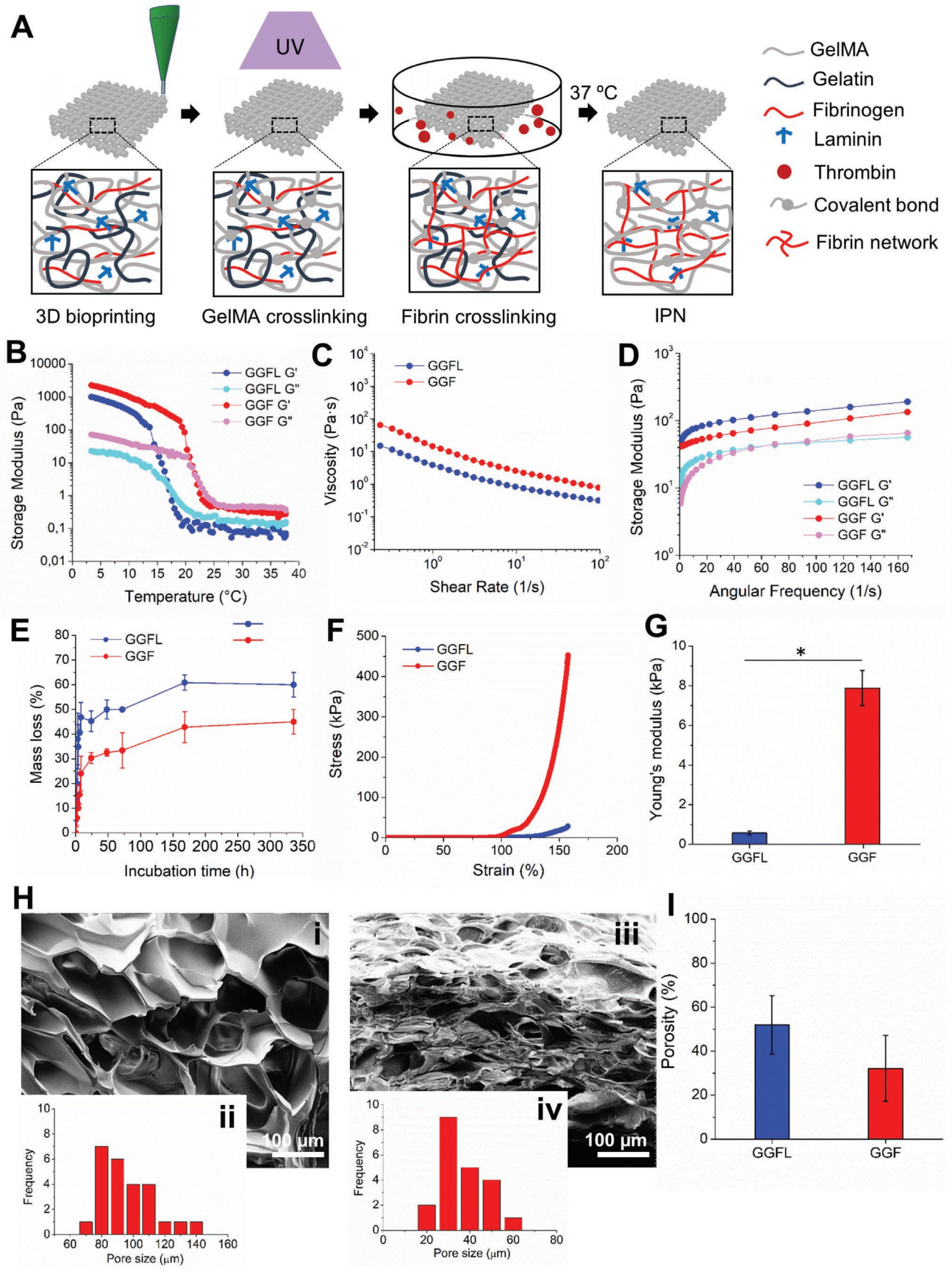

compressing the hydrogel's up to their rupture, with results showing increased stiffness and slightly less elasticity of GGF than GGFL, with elongation capacity of 156% and 158%, respectively (Figure 1F). Increased stiffness of GGF was corroborated by the Young's modulus evaluation, calculated from the stress versus strain curves, being 7.9 ± 0.9 kPa, significantly higher than GGFL (0.6 ± 0.1 kPa) (Figure 1G). These results indicate that GelMA networks contributed significantly to the hydrogel's stiffness, while the increase in fibrinogen concentration from 1.5 to 3 mg mL^{-1} maintained the material's softness. As we recently reviewed, fibrin is commonly used to mimic soft tissues.[42] Its mechanical properties can be tuned when fibrinogen concentration is increased to a wider range, as shown by Duong et al., that modulated fibrin networks stiffness to 5.5 kPa by increasing fibrinogen concentration to 50 mg mL^{-1}.[43] Nevertheless, for brain-like tissue, achieving mechanical modulus <1 kPa is highly favorable for neural cells scaffolding.

Each scaffold was analyzed for their morphology, pore size, and porosity via scanning electron microscopy (SEM). SEM images showed porous structures, with GGFL presenting larger and more round pores, while for GGF, pores were flat and consequently, of smaller size (Figure 1H). Despite the morphological differences, porosity did not change significantly between the hydrogels, although GGFL showed a tendency to an increased porosity (51.9 ± 13.3%), as compared to GGF (32.2 ± 15.0%) (Figure 1I), which is highly favorable for cells interconnection, homogeneous distribution, and nutrients and gaseous exchange.[44]

2.2. Characterization of Bioinks' Biological Properties

The biocompatibility of the mimetic microenvironment with the neural cells is crucial to obtain a functional neural-like tissue responding to SARS-CoV-2 infection similar to the in vivo model. For this, we used murine astrocytes mixed with GGF and GGFL, forming the bioinks, which were used to test cell viability, adhesion, spread, and expression of specific cell markers. Primary culture of astrocytes derived from C57Bl/6 mice is well established in the literature and has been a target cell type in regenerative neurobiology studies, including the biofabrication of 3D in vitro neural models.[45,46]

Initially, cells were mixed to the biomaterials' solution, bioprinted, and cultured at 37 °C and 5% of CO_2 (**Figure 2**A). The bioprinted structure possessed a squared shape, and cells were homogeneously distributed within the bioprinted layers (Figure 2B). Cell viability was assessed for 14 d using live/dead reagent, and results showed a significantly higher viability for astrocytes bioprinted and cultured in GGFL, as compared to GGF during the entire experiment (Figure 2C). After bioprinting (day 0), viability of astrocytes embedded in GGF was significantly lower than in GGFL (54.9 ± 0.5% and 78.1 ± 5.8%, respectively). During extrusion, cells will inevitably undergo shear stress, due to the cells-nozzle contact.[47,48] Besides, bioink's viscosity also directly influences on cell shear stress,[47] and then, controlling its rheology is crucial to assure proper cell functionality, once shear stress affect cell proliferation, signaling, and differentiation.[49,50] Our results showed that GGFL, which presented lower viscosity, was capable to protect the cells from a higher shear stress, assuring increased viability. With time, cell viability increased for both conditions, being 66.2 ± 4.9% (GGF) and 85.4 ± 3.3% (GGFL) on day 7 and 84.25 ± 4.5% (GGF) and 93.0 ± 2.9% (GGFL) after 2 weeks in culture. Although astrocytes viability reached 84% for GGF condition, cell adhesion and spread were poor (Figure 2D-i). On the other hand, astrocytes in GGFL presented higher adhesion, with an elongated and star-like shape, which is characteristic of astrocytes in 3D microenvironments,[51] suggesting higher matrix recognition and anchorage (Figure 2D-ii). This was corroborated by analyzing the presence of glial fibrillary acidic protein (GFAP), a specific marker expressed in mature astrocytes.[52] After 7 d of bioprinting, cells in GGF hydrogel expressed GFAP but maintained a rounded morphology (Figure 2E–i), which could be an indicative of functionality loss, a hallmark in many neural pathologies.[51] Differently, astrocytes in GGFL expressed GFAP (Figure 2E–ii) and presented a typical astrocyte morphology,[53] with circularity closer to zero (Figure 2F). These findings showed to be specifically due to the presence of laminin, an ECM component, used as a supplement in GGFL bioink, that contributed to neural cells adhesion and spread in scaffolds.[18] Although the IPN was composed of GelMA chains and fibrin fibers, two natural biopolymers commonly used in 3D cell culture that possess the specific recognition domain RGD (Arg-Gly-Asp) with high cell affinity, the presence of laminin seemed to be crucial to stimulate astrocyte native-like behavior. Therefore, the bioink GGFL was chosen for the biofabrication of the neural-like tissue, due to its favorable mechanical, physical, and biological properties.

2.3. In Vitro Serial Adaptation of SARS-CoV-2 Using Murine Neurospheres

Aiming to increase the permissiveness of the 3D bioprinted mice neural cells to SARS-CoV-2, a mouse-adapted virus was generated. A previous study demonstrated that induced pluripotent stem cell (iPSC)-derived neurospheres are permissive to SARS-CoV-2 infection and support productive virus replication.[10,12] In addition, neurospheres have being largely used as in vitro model in a variety of infection studies, including Zika virus (ZIKV) brain infection.[54,55] Thus, in this work, we

Figure 1. Optimization of bioink. A) Scheme of 3D bioprinting and crosslinking of gelatin-GelMA-fibrinogen bioinks. B) Temperature-dependent behavior of GGF and GGFL bioinks affecting the storage (*G'*) and loss (*G"*) moduli. C) Change of viscosity with shear stress of the bioinks. D) Variations in *G'* and *G"* of the bioinks with angular frequency showing their elastic behavior. E) Mass loss of GGF and GGFL hydrogels with time. F) Stress–strain curves of hydrogels up to fracture point. G) Young's modulus of hydrogels calculated from stress–strain curves ($n = 3$). *$p < 0.05$. H) SEM images of hydrogels at a magnification of 500 x, showing the materials' porosity (i) microscopy of GGFL, (ii) pore size histogram of GGFL, (iii) microscopy of GGF, and (iv) pore size histogram of GGF. Pore size was measured from at least 3 different images using ImageJ software. I) Porosity of hydrogels calculated from SEM images ($n = 3$). Statistical significance was analyzed by means of one-way ANOVA with Tukey's test.

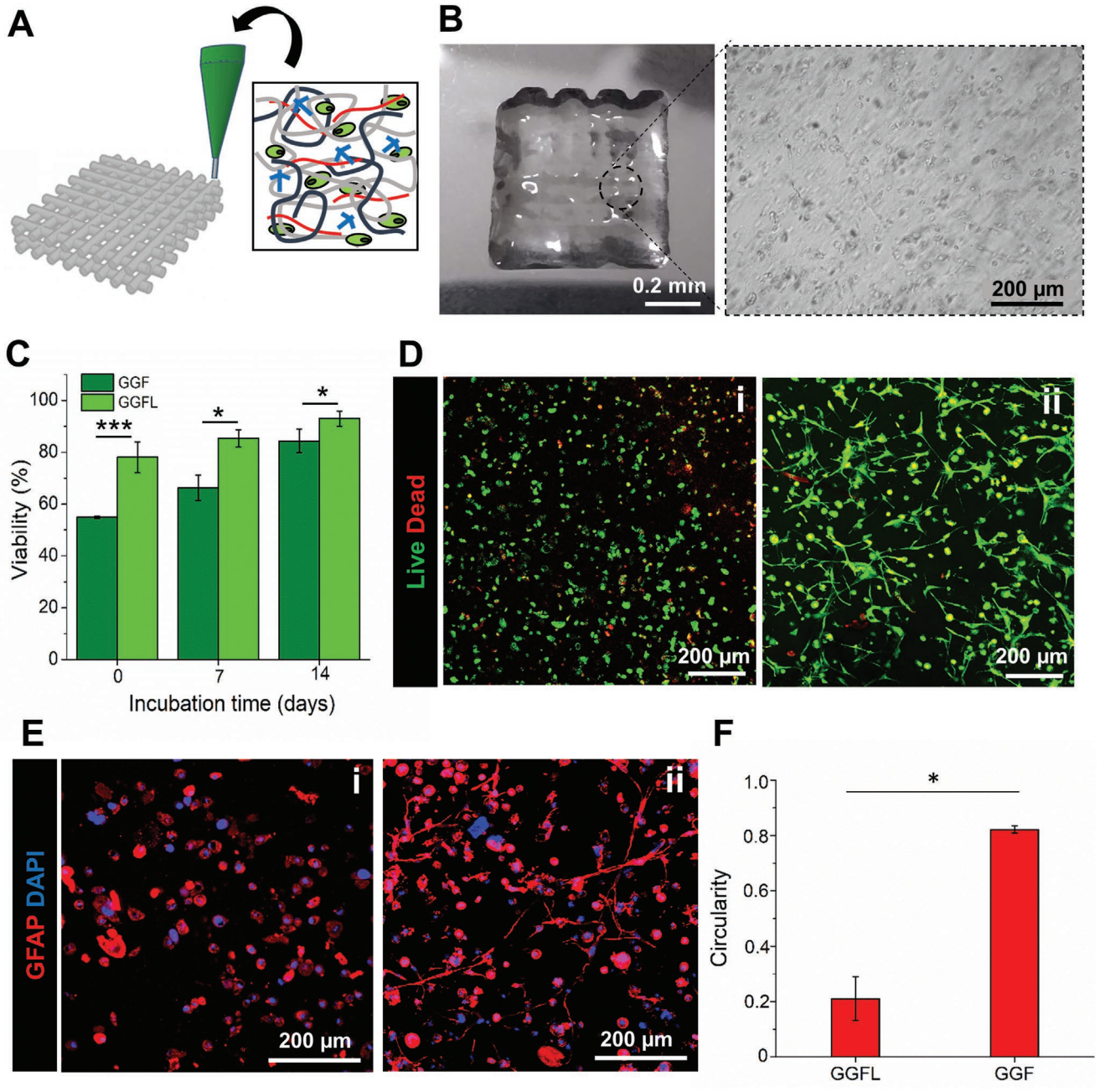

Figure 2. 3D bioprinting of astrocytes. A) Schematic illustration of astrocytes-laden GGFL bioink for 3D bioprinting. B) Image of a 3D bioprinted tissue and astrocytes homogeneously distributed within the structure. C) Viability of astrocytes bioprinted using GGF and GGFL bioinks ($n = 3$). $^{*}p < 0.05$ and $^{***}p < 0.01$. D) Images of astrocytes bioprinted in (i) GGF and (ii) GGFL bioinks and stained with live/dead reagent. E) Immunofluorescence of bioprinted astrocytes using (i) GGF and (ii) GGFL bioinks, stained for GFAP (red) and 4′,6-diamidino-2-phenylindole (DAPI) (nuclei, blue). F) Circularity of astrocytes calculated from immunofluorescence images of at least 3 images using ImageJ software. $^{*}p < 0.05$. Statistical significance was analyzed by means of one-way ANOVA with Tukey's test.

used mice-derived neurospheres to adapt SARS-CoV-2 in vitro (**Figure 3**A).

It is well known that SARS-CoV-2 host entry depends on ACE2,[4] which expression was demonstrated to be lower in brain as compared to other tissues, such as lung, intestine, liver, and heart.[56] Despite the similarities of ACE2 distribution in human and mouse brains,[21] ACE2 structure differs significantly between these two species, resulting in lower infection capacity of hSARS-CoV-2 in mice cells.[57] Murine neurospheres express ACE2 (Figure 3B), suggesting permissiveness to SARS-CoV-2, data consistent with Zhang et al. results.[12] This was corroborated by incubating neurospheres with hSARS-CoV-2. Forty-eight hours postinfection (hpi), a significant amount of infectious virus particles ($4.3 \pm 0.31 \times 10^2$ plaque-forming units (PFU) mL^{-1}) was released to the culture medium. However, the amount of infectious virus particles released by the murine

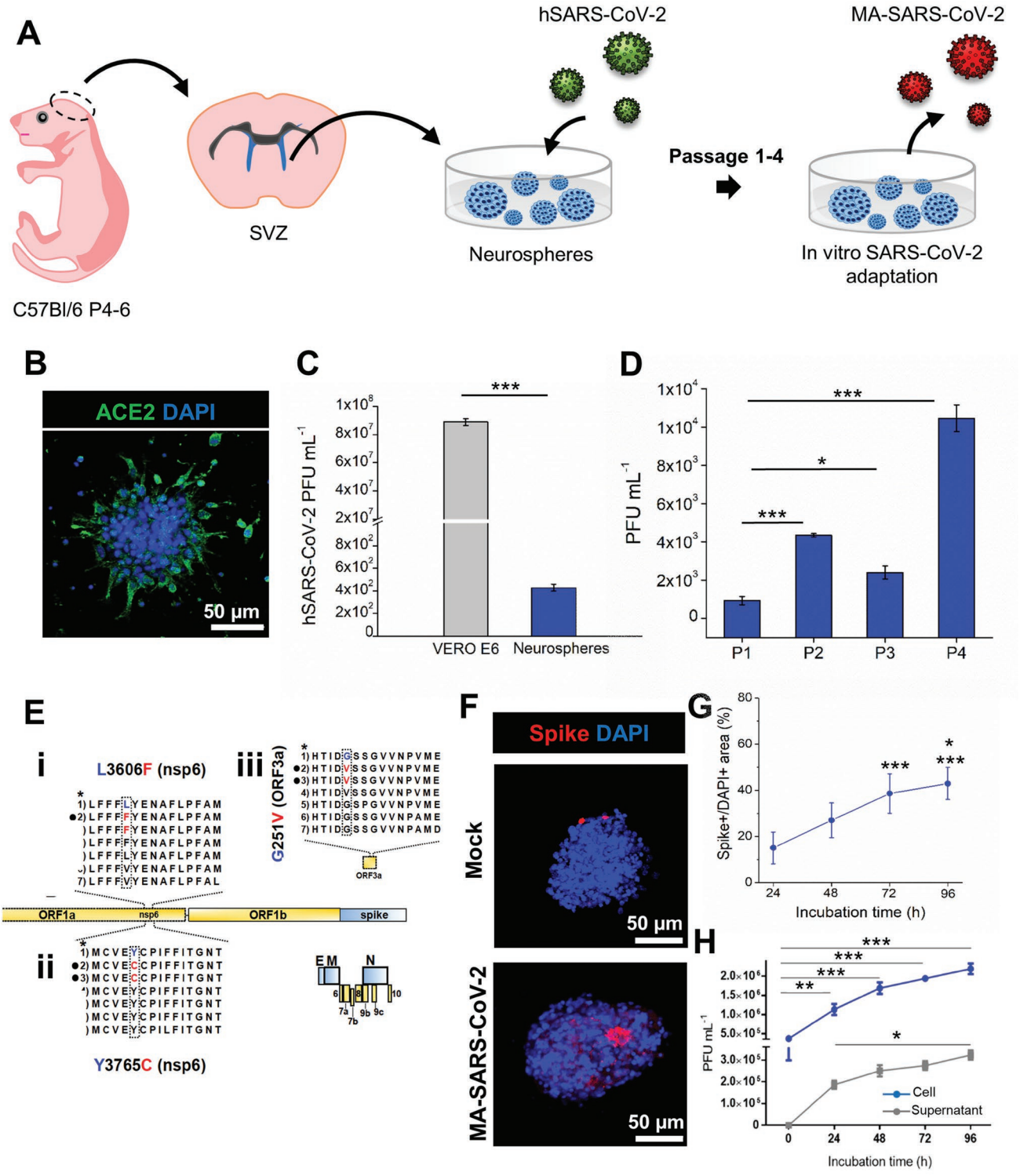

Figure 3. Mouse adaptation of SARS-CoV-2. A) Schematic illustration of the SARS-CoV-2 adaptation, in which the neurospheres were initially isolated from the SVZ of mice pups, and incubated with hSARS-CoV-2 until the generation of MA-SARS-CoV-2 after 4 passages. B) Immunofluorescence staining for DAPI (blue) and SARS-CoV-2 receptor ACE2 (green) in the mice-derived neurosphere. C) Titer of hSARS-CoV-2 48 hpi in Vero E6 cells and neurospheres ($n = 2$). $^{***}p < 0.01$. D) Titer of adapted SARS-CoV-2 for each passage 7 dpi in neurospheres ($n = 2$). $^{*}p < 0.05$ and $^{***}p < 0.01$. Statistical significance was analyzed by means of unpaired two-tailed Student's t test. E) Alignment of mutated regions of MA-SARS-CoV-2 (i) and (ii) mutations located at nsp6 (Orf1a) region, and (iii) mutations located at ORF3a region. In red, the putative amino acid substitutions in MA-SARS-CoV-2 and hSARS-CoV-2 used in the in vitro experiments. *Reference 1) Wuhan_CH (RefSeq) (NC_045512_2), 2) MA-SARS-CoV-2, 3) hSARS-CoV-2, 4) SARS-CoV-2_BR (EPI_ISL_413016), 5) SARS-CoV-2_BR_P.1 (EPI_ISL_1068292), 6) BatCoV_RaTG13 (MN996532.2), and 7) PCoV_GX-P5L (MT040335.1).

neurospheres was significantly lower than that released by Vero cells ($8.9 \pm 0.24 \times 10^7$ PFU mL^{-1}) (Figure 3C), indicating a lower permissiveness of the hSARS-CoV-2 to the mice-derived neural stem cells (NSCs).

hSARS-CoV-2 was then submitted to mouse adaptation, aiming to increase the specificity of the virus to murine cells. Differently from previous works that used in vivo models for mouse adaptation,[24,28,29] here we generated a mouse-adapted strain in vitro, which is a much simpler and a highly effective protocol. Neurospheres were incubated with hSARS-CoV-2 for 7 d, and the amount of virus particles recovered from the culture medium after this incubation period was $9.2 \pm 2.1 \times 10^2$ PFU mL^{-1}, a twofold increase in the amount detected at 48 hpi (Figure 3D). This passage was defined as P1, which was serially inoculated in a new batch of neurospheres. The level of infectious virus particles of SARS-CoV-2 at passages 2 and 3 (P2 and P3, respectively) increased significantly as compared to P1, remaining in the range of $2–5 \times 10^3$ PFU mL^{-1}. At passage 4 (P4), virus particles reached 10^4 PFU mL^{-1}, significantly higher than previous passages and P4 was used as the mouse-adapted SARS-CoV-2 (MA-SARS-CoV-2).

According to the maximum-likelihood phylogenetic analysis of the two sequenced genomes, MA-SARS-CoV-2 and hSARS-CoV-2 are closely related to the original Wuhan strain (reference sequence-NC_045512.2) (Figure S2, Supporting Information). Interestingly, MA-SARS-CoV-2 showed fewer mutations than the hSARS-CoV-2 (Figure 3E and Figures S3 and S4, Supporting Information) and we found three nonsynonymous mutations in MA-SARS-CoV-2 sequence. The same mutations are present in hSARS-CoV-2: two of them in ORF1a, specifically at nsp6 regions (Figure 3E–i,ii) and one in ORF3a region (Figure 3E–iii). However, hSARS-CoV-2 strain presents many other synonymous and non-synonymous mutations, including at the N protein region (Table S2, Supporting Information), which were reverted in the MA-SARS-CoV-2 genome, which is closer to the Wuhan reference sequence (NC_045512.2). These data reveals that MA-SARS-CoV-2 reverted some nonsynonymous mutations that the hSARS-CoV-2 virus probably acquired throughout its evolution in humans since the beginning of the pandemic when compared to the original Wuhan isolate.

Immunofluorescence analysis showed that neurospheres infected with MA-SARS-CoV-2, expressed the viral protein S (spike) (Figure 3F). In addition, growth kinetics of MA-SARS-CoV-2, measured by total area of spike$^+$ over DAPI$^+$ cells (Figure 3G) and viral load in cell and supernatant quantified by RT-qPCR (converted to PFU mL^{-1}) (Figure 3H), revealed significantly the capacity of virus production by the neurospheres over time.

These results evidenced that the mouse-adapted virus strain we generated in vitro using murine neurospheres was able to efficiently infect and reproduce in mice neural cells. The viral adaptation via passages in neurospheres could be critical, as it may result in the selection of a more neurotropic SARS-CoV-2 variant. For this work, the methodology was precisely chosen aiming the development of a model with tropism for CNS cells, suitable to study the mechanisms of pathogenesis in the tissue and cells of the nervous system. Currently, it is known that brain tropism and post-COVID-19 sequelae impair CNS functions, which appears to be the newest and emerging concern regarding COVID-19, in addition to the pathogenesis mechanisms responsible for post-COVID neurological sequelae[58–60] that are far from being well established.[61] Since the genome of the adapted virus is very similar to that of the virus isolated from humans used in the generation of MA-SARS-CoV-2, virus-host cell interactions are relevant to the in vivo context on which novel SARS-CoV-2 variants are selected. Many in vivo interactions between the virus and host cells do not depend only on mutations in the spike protein, which occur in the highest frequency in the majority of naturally selected variants among the human population.[62]

2.4. MA-SARS-CoV-2 Infection of Neural Cells in 2D and 3D Conditions

Aiming to validate the specificity of MA-SARS-CoV-2 towards murine cells, Vero E6 cells were infected with both mouse adapted and human strains. Immunolocalization of spike showed low infection capacity of MA-SARS-CoV-2, as compared to hSARS-CoV-2, indicating low specificity with the mouse-adapted virus to infect a primate cell line (Figure S5A,B, Supporting Information). Subsequently, MA-SARS-CoV-2 neurotropism was evaluated by infecting 2D culture of murine astrocytes and mature neurons. Microglia was not incorporated in the study design, as previous works reported a significantly lower expression of ACE2 in these cells as compared to primary human astrocytes,[63] in addition of no infection capacity[64] and lack of influence on SARS-CoV-2 survival and replication[65] being observed in 2D cultures of this glial cell type.

Immunostaining showed that MA-SARS-CoV-2 was efficient in infecting both murine cell types (**Figure 4**A), with mean pixel intensity of spike protein stain showing a significantly higher specificity for cells with the adapted virus as compared to hSARS-CoV-2 (Figure S6, Supporting Information). These findings suggest that mutations acquired by hSARS-CoV-2 along its evolutionary trajectory in the human host were lost or reversed after the in vitro adaptation in murine cells, giving rise to MA-SARS-CoV-2, which would explain its highest adaptability and ability to infect murine cells. The capability of the adapted virus in infecting murine astrocytes and neurons was expected, as we observed expression of ACE2 by both cells, analyzed by immunofluorescence (Figure S7A, Supporting Information) and mRNA expression, which showed no significant difference between both cell types (Figure S7B, Supporting Information).

F) Immunofluorescence staining for DAPI (blue) and SARS-CoV-2 spike protein (red) in neurospheres for mock condition (anti-spike negative control) and infected with MA-SARS-Co-2, from P4. G) Growth kinetics of MA-SARS-CoV-2 in neurospheres, measured from the total area of spike$^+$ over DAPI$^+$ cells, using the ImageJ software from at least three images of each replicate. ($n = 2$). $^*p < 0.05$ and $^{***}p < 0.01$, related to 24 h. H) Viral load cell (blue) and supernatant (gray) of growth kinetics of MA-SARS-CoV-2 in neurospheres, measured by RT-qPCR, using N viral primer. Data were shown in PFU mL^{-1} after linear regression analysis between PFU mL^{-1} titration results and Ct values from RNA curve constructed with each point of the serial dilution of the viral stock (Figure S5D). ($n = 2$) $^*p < 0.05$, $^{**}p < 0.001$ and $^{***}p < 0.0001$. Statistical significance was analyzed one-way ANOVA with Tukey's test.

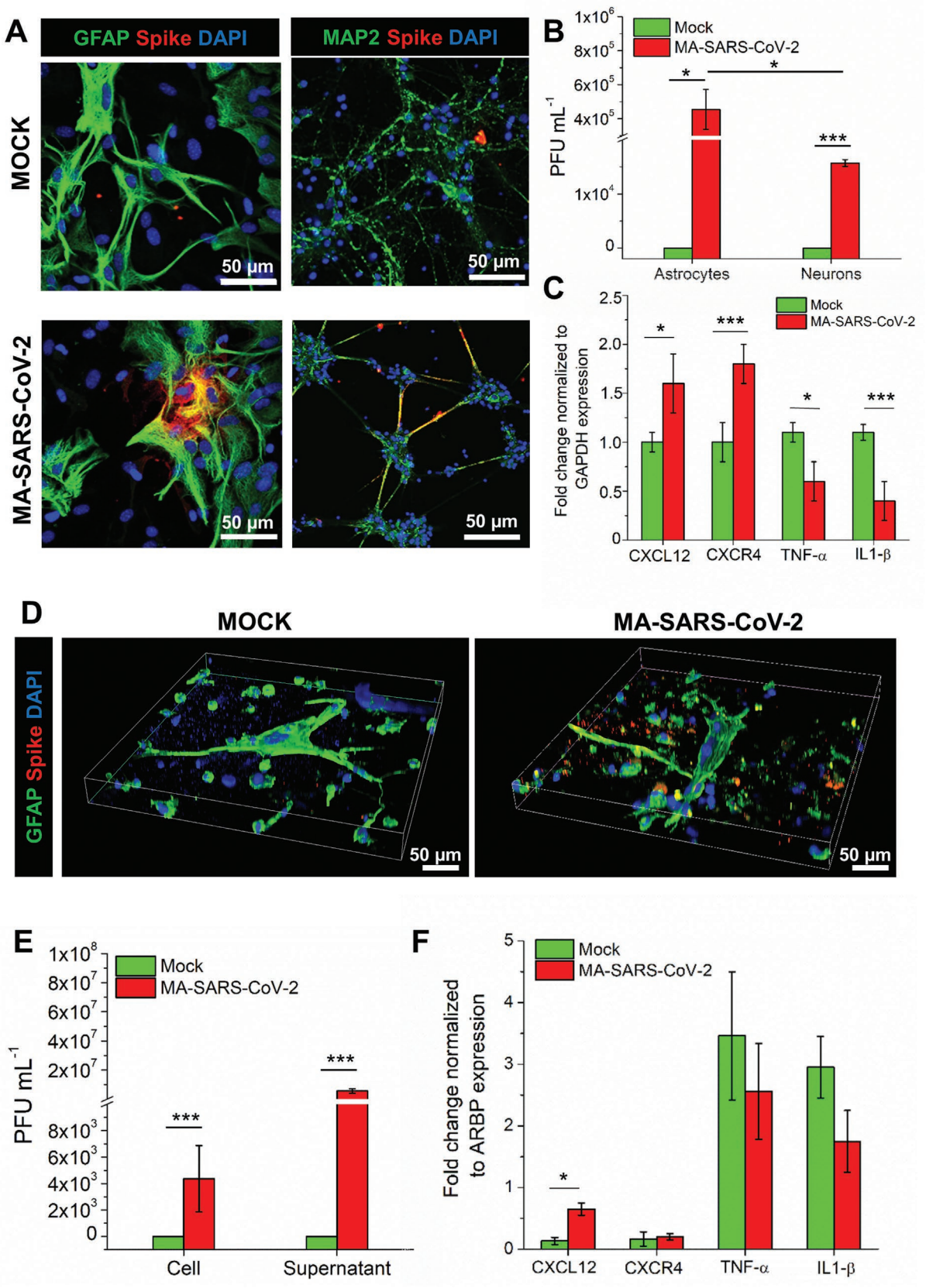

Despite this evidence, it was not possible to determine whether the mechanism of entry and infection of MA-SARS-CoV-2 in murine cells was actually due to the spike-ACE2 interaction, since the murine ACE2 protein has a lower affinity for the viral spike than its human counterpart.[66] However, similarly, ACE2 expression by murine primary astrocytes and mature neurons was also reported by Chen et al. in a study of the spatial distribution of ACE2 in mouse and human brain.[21] Other works suggested that neurons are not a primary site of infection in humans due to their low expression of ACE2,[67,68] while astrocytes were considered to be directly involved in SARS-CoV-2 neuropathogenesis, with an increased capacity to express the SARS-CoV-2 receptor.[21,69]

In addition to use ACE2 as for cell entry, SARS-CoV-2 needs a co-factor for spike priming, such as the transmembrane serine protease 2 (TMPRSS2) that facilitates the virus entry into host cells.[4] More recently, it was reported that neuropilin-1, a protein that binds furin-cleaved substrates, is also used by SARS-CoV-2 as spike priming,[70] enhancing the entry of the virus in the CNS.[71] Both cofactors, TMPRSS2 and neuropilin-1, were expressed by astrocytes and neurons (Figure S7B, Supporting Information), as also observed in previous works.[72,73]

Neuronal infection by MA-SARS-CoV-2 led to cell–cell fusion and the formation of neuronal syncytium (Figure 4A), corroborating the specificity of the mouse-adapted virus to this cell type, once this behavior was not observed for cells infected by hSARS-CoV-2 (Figure S6B-ii, Supporting Information). Spike protein present at the plasma membrane of cells is able to trigger syncytia formation, in which the cell–cell fusion is mediated by TMPRSS2.[74] As previously reported, syncytia formation was also observed in pneumocytes infected with SARS-CoV-2.[75] This behavior, similarly observed for neurons infected by Varicella-zoster virus,[76] suggests that SARS-CoV-2 infection might lead to neuronal malfunction. Infection of 2D cultures indicates that both cell types could potentially be used by the virus to infect the CNS, through ACE2/TMRPSS2 and ACE2/neuropilin-1 routes, contributing to virus spread in the brain.[77,78]

Results of immunostaining suggest that astrocytes present higher susceptibility to infection than neurons, with quantification of immunofluorescence for spike$^+$ cells over DAPI showing that 15.7 ± 2.9% of astrocytes were infected by MA-SARS-CoV-2, while for neurons, this value corresponded to 10.3 ± 2.1% (Figure S6A, Supporting Information). Similarly, Jacob et al. reported the ability of hSARS-CoV-2 to preferentially infect 2D culture of human primary astrocytes as compared to neurons, being observed sparse infection after 48 h.[64] Astrocytes also showed a significantly higher capacity to replicate the mouse-adapted virus than neurons, being analyzed 48 hpi. Results showed that astrocytes produced approximately 30-fold MA-SARS-CoV-2 virus particles than neurons, with values being $4.5 \pm 1.2 \times 10^5$ and $1.6 \pm 0.6 \times 10^4$ PFU mL^{-1}, respectively (Figure 4B). Here, mature neurons were able to replicate the virus, evidence also observed by Song et al., which suggested that SARS-CoV-2 may use neuron cell machinery for replication.[14] On the other hand, different works have reported a poor or no capacity of neurons to actively replicate the virus, even though they expressed ACE2[72] and were susceptible to SARS-CoV-2 entry.[11] However, it is relevant to point out the use of different cell sources and protocols of infection among these studies, which directly affect viral response.

Given the significantly higher infectivity of astrocytes as compared to neurons, our results suggest that astrocytes may play a major role in SARS-CoV-2 mechanisms of neurological manifestations of COVID-19,[79] contributing to virus spread and permanence, neurotoxicity, and reduction of metabolites, impairing neuronal viability and functionality, behavior observed when brain was infected by other viruses.[80,81]

In face of an injury, including viral infection,[82–84] astrocytes respond with reactivity, a mechanism that leads to the production of several inflammatory cytokines.[77] In order to evaluate the regulation of inflammation mediators by astrocytes after MA-SARS-CoV-2 infection, we characterized the expression of the inflammatory cytokines IL1-β and TNF-α, in addition to the expression of the chemokine CXCL12 and its receptor CXCR4. Results showed that MA-SARS-CoV-2 infection upregulated the expression of CXCL12 and CXCR4, while the inflammatory cytokines were downregulated in the infected astrocytes condition (Figure 4C). The increased expression of CXCL12 and its receptor CXCR4 in infected astrocytes as compared to mock, shows the response of astrocytes to MA-SARS-CoV-2 in controlling the inflammatory signals, as the main function of CXCL12 is to attract immune cells to injury sites.[85]

Due to the higher susceptibility of the glial cells to infection, bioprinted astrocytes were infected with MA-SARS-CoV-2, aiming to compare cellular and molecular behavior of 2D and 3D culture models after virus exposure. After 7 d of bioprinting and 48 hpi, immunostaining assay showed the presence of spike protein in the infected bioprinted tissue (Figure 4D), with an increased permissiveness as compared to the mock-infected cells and infection with hSARS-CoV-2, as showed by measures of mean pixel intensity (Figure S8A,B, Supporting Information). Quantification of spike$^+$ cells over DAPI revealed that 13.4 ± 2.9% of bioprinted astrocytes were infected by MA-SARS-CoV-2, slightly lower than astrocytes in 2D culture, while for the human strain, this value was 8.9 ± 0.2% (Figure S8C, Supporting Information). Similarly, Jacob et al. used an organotypic

Figure 4. Infection of 2D and 3D neural cultures with MA-SARS-CoV-2. A) Immunofluorescence images of (i) astrocytes stained for nuclei (DAPI, blue), GFAP (green), and spike protein (red) and (ii) neuronal 2D culture stained for nuclei (DAPI, blue), MAP2 (green), and spike protein (red), infected with mock and MA-SARS-CoV-2, 48 hpi. B) Titer of MA-SARS-CoV-2, 48 hpi ($n = 2$). $^*p < 0.05$ and $^{***}p < 0.01$. C) Chemokines and inflammatory cytokines expressed by astrocytes infected with MA-SARS-CoV-2, 48 hpi ($n = 3$). $^*p < 0.05$ and $^{***}p < 0.01$. B,C) Statistical significance was analyzed by means of unpaired two-tailed Student's t test and one-way ANOVA with Tukey's test. D) Immunofluorescence images of 3D bioprinted astrocytes infected with mock and MA-SARS-CoV-2 stained for nuclei (DAPI, blue), GFAP (green), and spike (red). E) Virus titration in cells and supernatant for 3D bioprinted astrocytes infected with MA-SARS-CoV-2, 48 hpi, ($n = 3$). $^{***}p < 0.01$. Statistical significance was analyzed by means of one-way ANOVA with Tukey's test. F) Chemokines and inflammatory cytokines expressed by 3D bioprinted astrocytes infected with MA-SARS-CoV-2, 48 hpi ($n = 3$). $^*p < 0.05$. Statistical significance was analyzed by means of unpaired two-tailed Student's t test.

model to evaluate the infective capacity of the virus in astrocytes within a 3D structure, observing sparse infection, with no significant difference from that of 2D culture.[64] These findings indicate a lower capacity of the virus to infect 3D bioprinted astrocytes as compared to the 2D culture. This is probably due to the physical barrier the IPNs provided in the 3D model, not present in the monolayer, where cells are directly exposed to the virus. Therefore, results found for the 3D bioprinted tissue may be more representative of the in vivo system. Furthermore, virus titration for bioprinted astrocytes infected with MA-SARS-CoV-2 revealed the presence of $4.4 \pm 2.5 \times 10^3$ PFU mL^{-1} virus particles on cells, with $5.7 \pm 1.5 \times 10^6$ PFU mL^{-1} being produced after 48 hpi (Figure 4E).

Aiming to characterize the neuroinflammation potential of bioprinted astrocytes after MA-SARS-CoV-2 infection, the expression of the inflammatory cytokines IL1-β and TNF-α and the chemokine CXCL12 and its receptor CXCR4, was also evaluated. For the 3D samples, results showed a similar behavior to that of 2D culture (Figure 4F). Nevertheless, it was observed an increase in the expression of both inflammatory cytokines, especially TNF-α, as compared to the 2D culture. The ECM plays important role in astrocytes functionality, including directly affecting the cellular response to inflammatory signals.[86] Therefore, the 3D microenvironment of the bioprinted structures seemed to regulate inflammation after infection, suggesting a better recapitulation of astrocytes response in vivo.

2.5. MA-SARS-CoV-2 Infection of Biofabricated Neural-Like Tissue

In order to increase the complexity of the 3D neural-like tissue, mature neurons (MAP2$^+$) (Figure S9, Supporting Information) were seeded on the top of the bioprinted astrocytes, being incorporated into the structure during tissue maturation (**Figure 5**A). Due to the inherent sensitivity of neurons, the extrusion of this cell type leads to low viability, assessed by testing different bioprinting and crosslinking conditions, such as speed (Figure 5B) and time of UV exposure (Figure 5C), with significantly lower viability when compared to bioprinted astrocytes. As it is well known, mature neurons do not proliferate,[87] and the low number of cells could compromise response to infection. Therefore, commonly used strategies to biofabricate platforms for neuronal studies in vitro is to bioprint neural stem cells and stimulate their neuronal differentiation within the structure,[18] or to seed neurons on previously bioprinted and crosslinked samples.[88] In this work, we used the second approach, aiming to construct a heterogeneous neural-like tissue to be used as an in vitro model suitable for MA-SARS-CoV-2 infection.

After 7 d of astrocytes bioprinting, 1×10^4 mature neurons were seeded on the top of the structure, that previously received an extra coating with laminin in order to increase neuronal adhesion, cultured in a 1:1 ratio of astrocytes and neurons media. Immunostaining performed after 7 d of culture showed that neurons were incorporated into the bioprinted structure, connecting with astrocytes on the top (Figure 5D-i) and z direction (Figure 5D-ii), with cells expressing GFAP and β-tubulin III, specific markers for astrocytes and neurons, respectively. These images show that we were able to biofabricate a heterogeneous neural-like tissue using murine primary astrocytes and neurons.

As reported in previous works, 3D models such as neural organoids and assembloids showed to be suitable platforms to study SARS-CoV-2 infection in the brain.[8,12,13,64] However, these models are formed from the spontaneous aggregation of embryonic stem cells or iPSCs, in an uncontrolled and unpredictable manner. Biofabrication strategies, such as 3D bioprinting, allows greater control and assembly, directing cell organization.[89]

The biofabricated neural-like tissue was infected with MA-SARS-CoV-2, and immunostaining images showed a significant increase of spike protein presence for the sample infected with the mouse-adapted virus, as compared to the mock-infected cells (Figure 5E) and human strain, determined by mean pixel intensity (Figure S10A,B, Supporting Information). Values obtained from immunofluorescence quantification of spike$^+$ cells over DAPI revealed that $15.9 \pm 2.6\%$ of cells were infected by MA-SARS-CoV-2, a value slightly higher than that of bioprinted astrocytes, indicating a lower contribution of neurons to increase the infectivity of the biofabricated tissue. Besides, infection of the 3D tissue with MA-SARS-CoV-2 did not lead to neuronal syncytium formation, differently from what we found for the 2D model and from that observed previously in organotypic models.[64]

Cells infected by hSARS-CoV-2 and mock-infected cells represented $4.1 \pm 2.0\%$ and $2.7 \pm 1.0\%$, respectively (Figure S10C, Supporting Information). Besides, the neuronal population in cortical organoids showed to be only minimally infected by SARS-CoV-2, with astrocytes being the main targeted cells.[90] MA-SARS-CoV-2 particles found in cells were $0.85 \pm 0.3 \times 10^3$ PFU mL^{-1}, being able to replicate 48 hpi, with virus particles in the supernatant being $1.96 \pm 0.2 \times 10^3$ PFU mL^{-1} (Figure 5F). Bauer et al. reported low presence of the virus in neurons/astrocytes coculture.[72] Here, the presence of neurons in the 3D structure seemed not to affect the capacity of the virus to infect the tissue, when comparing to results obtained for bioprinted astrocytes.

These findings support the evidences that astrocytes might be directly involved in SARS-CoV-2 neuropathogenesis,[77,91] although the literature remains controversial. Organoids have been the most used 3D model to study SARS-CoV-2 neurotropism, with some results indicating that astrocytes were preferentially infected by the virus with poor neuronal infection capacity,[64,90] while other works reported neurons as the main target of SARS-CoV-2.[11,92] Notably, the heterogeneity of organoids due to self-organization may contribute to the reported variability among studies.[90] Therefore, the 3D bioprinting technology can overcome this challenge and contribute to a more standardized neural-like tissue biofabrication to study SARS-CoV-2 neurotropism. The optimization of bioink, IPN characterization, and standardization of bioprinting procedure presented here paves the way for the biofabrication of more complex neural-like structures, which will allow the incorporation of other cell types and important components of the brain tissue, such as the blood-brain barrier (BBB) and blood-cerebrospinal fluid barrier (BCSFB). As several studies have reported, the components of BBB and BCSFB, such as pericytes, endothelial cells, and choroid plexus epithelium,

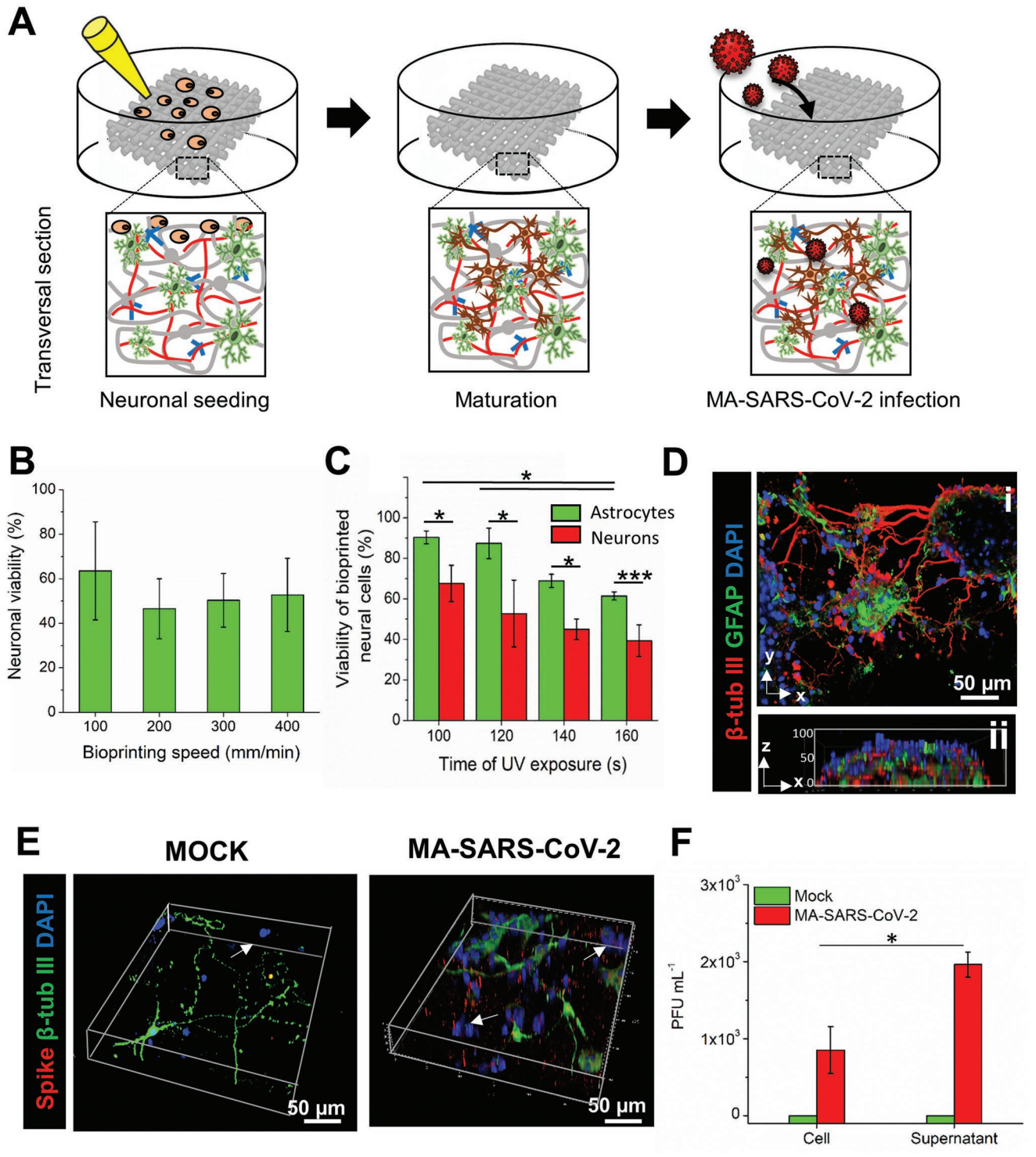

Figure 5. MA-SARS-CoV-2 infection of biofabricated neural-like tissue. A) Schematic illustration showing the construction of the 3D neural-like platform, by seeding murine neurons on the top of 3D bioprinted astrocytes, cell maturation, and MA-SARS-CoV-2 infection. B) Viability of 3D bioprinted neurons at different bioprinting speeds, ($n = 3$). C) Comparison of viability of bioprinted astrocytes and neurons after GelMA crosslinking using different UV exposure times, ($n = 3$). $^{*}p < 0.05$ and $^{***}p < 0.01$. Statistical significance was analyzed by means of one-way ANOVA with Tukey's test. D) Immunofluorescence showing (i) x-y and (ii) z-x images of the neural-like tissue stained for nuclei (DAPI, blue), GFAP (green), and β-tubulin III (red) after 7 d of culture. E) Immunostaining of 3D neural-like tissues infected with mock and MA-SARS-CoV-2, 48 hpi, stained for nuclei (DAPI, blue), β-tubulin III (green), and spike protein (red). White arrows are pointed to astrocytes. F) Virus titration in cells and supernatant for neural-like tissue infected with MA-SARS-CoV-2 strain, 48 hpi, ($n = 3$). $^{*}p < 0.05$. Statistical significance was analyzed by means of one-way ANOVA with Tukey's test.

primarily express ACE2, being the main target of SARS-CoV-2 in the CNS, especially, the choroidal epithelium.[8,13,64,93] The incorporation of microglia in further biofabricated neural-like tissues would also contribute to the generation of a more complex model, and although these cells are poorly infected by the virus, they might contribute to the understanding of the overall impact of SARS-CoV-2 brain infection.[77]

Furthermore, evidences have suggested that CNS SARS-CoV-2 invasion occurs at the neural-mucosal interface, with the virus being transported along the olfactory tract via axonal transport.[94] Analysis of the olfactory mucosa of deceased COVID-19 patients showed that sustentacular cells, which possess glial-like properties, are major SARS-CoV-2 target cells.[95] In line with this, even more complex systems can be developed using the 3D bioprinting strategy proposed here, such as the engineering of interconnected neural-mucosal interface, for ultimately understand the mechanisms of infection and neurotropism of SARS-CoV-2 in the CNS.

3. Conclusions

The complexity of the CNS poses a major challenge for the assessment of the neurological effects of SARS-CoV-2. The use of animal models and in vitro platforms are powerful tools for elucidating the underlying mechanisms governing brain infection, which remains inconclusive. In this work, we reported the biofabrication of a 3D neural-like tissue using bioinks with tunable biophysical properties and murine neural cells, useful as a proof-of-concept to study SARS-CoV-2 neurotropism. The virus specificity was obtained by in vitro adaptation, that lead to the generation of the MA-SARS-CoV-2 strain, using a protocol firstly reported in this work. The mouse-adapted SARS-CoV-2 showed high specificity to murine cells, being valuable to characterize the pathological effects of the virus in brain and other organs. Notably, MA-SARS-CoV-2 was effective to infect the 3D neural-like tissue. In future works, we aim to increase the complexity of the neural-like tissues using the 3D bioprinting technology and hiPSCs-derived neural cells. In addition, the engineering strategy proposed in this study allows the incorporation of BBB and BCSFB systems to mimic specific neurogenic niches, and the neural-mucosal transport interface, which will contribute to the understanding of the CNS virus entry. We envision that the use of 3D bioprinting to biofabricate highly complex systems under controlled conditions will improve research regarding the effects of COVID-19 in the CNS and allow the understanding of important cell behavior during brain infection, potentially contributing to the development of new treatments.

4. Experimental Section

Cell Lines: Simian kidney cell line Vero E6 (ATTC # CRL1586; P2), was kindly provided by Professor José Luiz Proença Módena from University of Campinas (UNICAMP), São Paulo, Brazil. Cells were cultured in MEM (Gibco, USA) supplemented with 10% fetal bovine serum (FBS) (Gibco) and 1% ampicillin/streptomycin antibiotics (Gibco) at 37 °C in a 5% CO_2 atmosphere until reaching 90% confluence.

Primary Cultures: C57Bl/6 mice pups were obtained from the Animal Facility (CEDEME/UNIFESP) and were manipulated following internationally approved protocols and in accordance with the Ethics Committee for Animal Research at UNIFESP (CEUA n. 2063220420). The number of animals and their suffering were reduced at its lowest. Neural stem cells were obtained from the SVZ of neonate C57Bl/6 pups (postnatal days 4–6) according to a protocol adapted from ref. [96]. Briefly, the animals were decapitated, and after carefully removing the brain from skull, the SVZ was microdissected and cells were enzymatically dissociated by incubation with Accutase (Gibco), followed by mechanical dissociation using a pipette. Then, the neural stem cells were plated on a six-well plate precoated with poly(2-hydroxyethyl methacrylate) (PolyHema) (Sigma-Aldrich, USA) at a density of 2×10^6 cells per well. Neural stem cells were cultured in DMEM/F12 (Gibco) supplemented with 2% glutamine (Sigma-Aldrich), 2% B27 (Invitrogen, USA), 20 ng mL^{-1} EGF (Sigma-Aldrich), 20 ng mL^{-1} FGF (Gibco), 5 µg mL^{-1} heparin (Sigma-Aldrich), and 1% penicillin/streptomycin (P/S) (Gibco). Neurosphere formation takes up to 10 d to occur, and during that time, culture medium was changed every 4 d by centrifugation, with half of the medium being replaced by fresh medium. Neurospheres were kept in an incubator at 37 °C and 5% CO_2. When neurospheres achieved a diameter of 50–100 µm after the P3, they were used in the infection studies. For primary astrocytes and neurons isolation, C57Bl/6 neonate pups (postnatal day 1) were decapitated, and after carefully removing the brain, the cortex was dissected and enzymatically digested with 0.005% trypsin (Gibco), followed by mechanical dissociation using a pipette. After enzyme inactivation, cells were centrifuged and the supernatant containing neurons was separated and cultured in a six-well plate at the density of 2×10^6 cells per well with Neurobasal medium (Gibco) supplemented with 2% B27, 1% glutamine, and 1% P/S. The pellet containing astrocytes were suspended in DMEM/F12 culture medium supplemented with 2% glutamine, 10% FBS, and 1% P/S. Cells were kept in an incubator at 37 °C and 5% CO_2. On the following day, medium was completely replaced, then half-medium was changed every third day. After 7 d in culture, neurons were used in the infection studies. Astrocytes from passages 2–3 at 90% confluency were used in the infection studies.

Virus Strain: The strain was originally isolated from the nasopharyngeal sample of a Brazilian patient (EPI_ISL_413016) with the sequence deposited in GenBank (accession no. MT 126808). The donated from P2 was amplified in a BSL3 laboratory to the P3 in Vero E6 cells, and virus titration was determined by plate-dilution assay as described.[97] A titer of 5×10^7 PFU mL^{-1} was obtained and stored at −80 °C. The generation of MA-SARS-CoV-2, in vitro passaging, and infection experiments were performed under BSL3 environment, following Pan American Health Organization (PAHO) and WHO recommendations.

Adaptation of SARS-CoV-2: The hSARS-CoV-2 P3 was used for viral adaptation in murine SVZ-derived neural stem cells culture as neurospheres. SVZ-derived neurospheres (approximately 800 neurospheres of 100–150 µm) were infected with a MOI of 0.2 of SARS-CoV-2, diluted in MEM with 1% FBS and incubated for 2 hours at 37 °C and 5% CO_2. Next, the neurospheres were rinsed with PBS for removal of attached viral particles and MEM with 10% FBS was added to the cultures. Infected cells were incubated for 5 d and then, the supernatants were harvested. After viral quantification, the harvested from first murine-passage supernatant was used to infect a new batch of neurospheres, generating the second murine-passage of SARS-CoV-2, and successively, until the generation of the fourth murine-passage (MA-SARS-CoV-2 P4).

Infection of Neural Cells with SARS-CoV-2: Murine cortical astrocytes and mature neurons, isolated from murine cortex (P4-6), in a concentration of $1{\times}10^4$ cells, were infected with a MOI of 0.2 of SARS-CoV-2 (P3) or MA-SARS-CoV-2 (P4). Infected cultures were kept for 2 h at 37 °C and 5% CO_2 in MEM with 1% FBS. Then, the cells were rinsed with PBS 1× to remove attached viral particles and fresh MEM with 10% FBS was added to the cultures. The cultures were interrupted after 24 or 48 h for subsequent analysis.[4]

Growth Kinetics of Infection of Neural Cells with SARS-CoV-2: Neurospheres, isolated from murine cortex (P4-6), in a concentration of

1×10^4 cells, were infected with a MOI of 0.2 of MA-SARS-CoV-2 (P4). Infected cultures were kept for 2 h at 37 °C and 5% CO_2 in MEM with 1% FBS. Then, the cells were rinsed with PBS 1× to remove attached viral particles and fresh MEM with 10% FBS was added to the cultures. The cultures were interrupted after 24, 48, 72, and 96 h for subsequent viral cell and supernatant analysis.[4]

Viral Titer Assessment and Tissue Viability: Viral titer in Vero E6 and viral load was evaluated by plaque assay and quantitative RT-PCR (qPCR) respectively (Figure S5C,D, Supporting Information), using the assay previously described by.[98] The cycle threshold (Ct) values were converted to PFU mL^{-1} using a quantitative RNA curve constructed with each point of the serial dilution of the viral stock used to determine PFU mL^{-1} titer. RNA was extracted from the culture supernatants using viral QIAamp Viral RNA Mini Kit (Qiagen, USA). Total RNA was extracted from cells using RNA total RNeasy Micro Kit (Qiagen). Already in plaque assay, Vero E6 were infected untitled or titled (10^{-1}, 10^{-2}, 10^{-3}, and 10^{-4}) MA-SARS-CoV-2. After 1 h of infection, 2% of CMC (Carboxymethyl Cellulose) was added to the supernatant and cultures were interrupted after 72 h of incubation, by PFA 4% fixing. Then, cells were stained by blue methylene, and quantification was made visually (Figure S5C, Supporting Information). Viral load of untitled MA-SARS-CoV-2 was made in parallel by RT-qPCR (Figure S5D, Supporting Information).

MA-SARS-CoV-2 Sequencing and Gene Expression: RNA of infected samples was extracted from an aliquot of 500 µL using the QIAamp Viral RNA Mini Kit (Qiagen) according to manufacturer's instructions, and its quality was assessed with the spectrophotometer NanoVue Plus (GE Healthcare, UK). SARS-CoV-2 was detected by real-time RT-PCR utilizing the Allplex 2019-nCoV Assay (Seegene Inc., Korea) and inflammatory genes detected by qPCR were performed using Fast SYBR Green Master Mix (Applied Biosystems, USA) in a 7500 real-time PCR System (Applied Biosystems). RNA was subjected to reverse transcription with the SuperScript III First-Strand Synthesis System (Thermo Fisher Scientific Inc., USA), and then incubated with the Ion AmpliSeq SARS-CoV-2 Research Panel (Thermo Fisher Scientific Inc.). The number of amplification cycles was adjusted based on the Ct of the N genes. For sequencing, products generated by target amplification reactions were subjected to a library preparation using the Ion AmpliSeq Library Kit Plus (Thermo Fisher Scientific Inc.), according to manufacturer's instructions. GAPDH or ARBP were used as a normalizer for gene expression and the $2^{\Delta\Delta Ct}$ method was used for relative quantification analysis of the transcripts.[99] The primer sequences are presented in Table S3 (Supporting Information).

Sequence Data, Spatial Distribution and Assignments for SARS-CoV-2: Briefly, newly-sequenced FASTQ data from distinct strains were submitted to the augur-based workflow, Nextstrain,[100] a viral genome database hosting a bioinformatics toolkit for evolutionary analyses based on sequence alignment by MAFFT,[101] followed by maximum-likelihood phylogenetic (IQ-Tree),[102] and phylodynamics analyses (TreeTime).[103] In order to compare the results to the data about SARS-CoV-2 variants across the world and their respective references ($n = 2752$), phylogenetic placement and clade assignments were performed using Nextclade v.0.13.0 (https://clades.nextstrain.org/), an interactive visualization platform for real-time tracking of pathogen evolution (https://nextstrain.org/). Mutations calling along the genome, which encompass major nucleotide and amino acid substitutions, were mapped and compared with the emerging SARS-CoV-2 variants through Sequence and Genome annotation views, a schema of the corresponding sequence by highlighting the differences to the reference Wuhan-Hu-1 strain (GenBank accession no. NC_045512.2), and rectangular phylogeny. Less frequently mutated residues were also explored.

Bioinks Preparation and Crosslinking: GelMA was synthesized according to the recently published protocol.[45] Two bioinks were prepared: GGFL, composed of gelatin (Sigma-Aldrich) 4% (m/v), GelMA 2% (m/v), fibrinogen (Sigma-Aldrich) 3 mg mL^{-1}, and laminin 2 µg mL^{-1}, and GGF, composed of gelatin 5% (m/v), GelMA 5% (m/v), and fibrinogen 1.5 mg mL^{-1}. Briefly, gelatin and GelMA were diluted in PBS 1×, and fibrinogen previously prepared in saline solution was mixed to the gelatin-GelMA emulsion until the established concentrations. Photoinitiator Irgacure 2959 (Sigma-Aldrich) was added to the bioinks at the concentration of 0.5%. GelMA crosslinking was made by exposing the construct to ultraviolet (UV) light at 2 mW cm^{-2} for 2 × 60 s (up and down), being followed by fibrin crosslinking by soaking the construct in a solution composed of 1 U mL^{-1} thrombin (Sigma-Aldrich) and $CaCl_2$ (10%, m/v) in a ratio of 90:1 (thrombin to Ca^{2+}).

Rheology Assays: Rheological properties of bioinks were measured by using a cone-and-plate measurement geometry (CP50-1) with a 50 mm diameter and 0.9815° cone angle in an Anton Paar MCR-102 Modular Compact Rheometer. The thermal ramp rate decreased from 38 °C to 3 °C in a cooling rate of 1 °C min^{-1}, carried out at an angular frequency of 10 rad s^{-1} and tension within the linear regime. The shear viscosity curves were obtained in a range of shear rate from 0.01 to 1000 s^{-1}. The frequency sweep measurements were performed within the linear viscoelastic region (LVER) in an angular frequency ranging from 0 to 180 rad s^{-1}. The tests were performed in triplicate ($n = 3$).

Mechanical Characterization: Crosslinked materials were submitted to mechanical compression using a TA.XT.Plus Texture Analyzer, equipped with 50 N load cell and a cylindrical probe of 12 mm diameter. Constant speed of 1 mm s^{-1} was applied in the hydrated samples measuring 10×10×3 mm, until the rupture point. Young's modulus was calculated from the slope of the stress-elongation curve between 1 and 1.5 loading. The tests were performed in triplicate ($n = 3$) at room temperature.

SEM Analysis: The microscopic structure of crosslinked hydrogels was carried out by freezing the samples at -80 °C for at least 2 d and drying them in an L-101 lyophilizer (Liotop, Brazil). After treating the samples with gold coating on POLARON Sputter Coater, SC7620 (VG Microtech, England), images were obtained using a LEO Electron Microscopy/Oxford microscope (Zeiss, Germany).

Physical Characterization: For degradation assay, crosslinked samples were lyophilized, and the dry weights (W_i) were measured. Afterward, samples were immersed in PBS 1× and at predetermined times, samples were lyophilized and weighted (W_f). Degradation was expressed as mass loss by (%) = $(W_f - W_i)/W_i \times 100$. Porosity was determined by immersing lyophilized samples in ethanol overnight, and measuring the ratio between the void volume (V_v) and the volume of dried samples (V_d): (%) = $V_v/V_d \times 100$. The pore size of hydrogels was determined by measuring at least 100 pores of at least 3 different SEM images, by using the ImageJ software. All experiments were performed in triplicate ($n = 3$).

Bioprinting Neural-Like Tissue: For bioprinting, 1×10^6 murine astrocytes (P1-P3) were mixed to 1 mL of bioink and transferred to a 5 mL syringe, avoiding bubbles formation. A 22-gauge blunt needle was connected to the syringe, which was placed in the printhead of a 3D bioprinter (3D Biotechnology Solutions, Brazil). Bioprinting was performed using a speed of 400 mm min^{-1} and 25 °C, under G-code control, using extrusion code (*E*) to 0.01 mm. After bioprinting and crosslinking, the constructs were transferred to a 24-well plate and cultured with astrocytes culture medium at 37 °C and 5% CO_2, changing the medium every three days. After 7 d of culture, the medium was removed, and the bioprinted constructs were soaked on 30 µg mL^{-1} laminin solution. Then, 1×10^4 murine mature neurons were seeded on the top of the bioprinted constructs. The culture medium was composed of astrocytes and neuronal medium in a ratio of 1:1. The constructs were incubated at 37 °C and 5% CO_2, with medium being changed every 3 d.

Infection of 3D Bioprinted Structures: A MOI of 0.2 of SARS-CoV-2 or MA-SARS-CoV-2 was used to infect the 3D bioprinted structures containing approximately 1×10^4 bioprinted primary astrocytes and 1×10^4 seeded mature neurons, both isolated from cortex of mice pups (P4-6) in each construct. Infected cultures were kept for 2 h at 37 °C and 5% CO_2 in astrocytes-neuronal medium (ratio of 1:1). Then, the constructs were rinsed with PBS 1× to remove attached viral particles and fresh medium was added to the culture, being interrupted after 48 h for subsequent analysis.

Immunocytochemistry Analysis: The 2D cultured cells were fixed in paraformaldehyde (PFA) 4% for 20 min, and 3D bioprinted cells were fixed for 2 h. Fixed cells were incubated with 0.1 mol L^{-1} glycine (Sigma-Aldrich) for 15 min and permeabilized with 0.1% Tween 20 (Sigma-Aldrich) for 10 min. Then, cells were blocked with 5% FBS in PBS for 1 h at room temperature and then incubated with primary antibodies at 4 °C overnight. Incubation with the appropriate secondary antibody and DAPI (1:10000, Molecular Probes, USA) was performed at room temperature for 1 h. Glass slides were mounted using Fluoromount G mounting medium (Electron Microscopy Sciences, USA). Bioprinted constructs were placed on a confocal dish for analysis. Images were captured on a Leica TCS SP8 confocal microscopy using LASAF software (Leica, Germany). Primary antibodies: mouse anti-spike S1 (1:100, Genetex, USA); rabbit anti-MAP2 (1:500, Millipore, USA); rabbit anti-βtubIII (1:500, Millipore, USA), chicken anti-GFAP (1:500, Abcam); goat anti-ACE2 (1:500). Secondary Antibodies (Invitrogen, USA): Alexa Fluor 488-conjugated goat anti-mouse IgG (1:500); Alexa Fluor 488-conjugated goat anti-chicken IgG (1:500); Alexa Fluor 488- conjugated goat anti-rabbit IgG (1:500), Alexa Fluor 594-conjugated goat anti-mouse IgG (1:500), and Alexa Fluor 594-conjugated goat anti-chicken IgG (1:500). Anti-spike specificity was assured by using mock-infected mice-derived neurospheres as the negative control and Vero E6 cells as the positive control.

Statistical Analysis: All experiments were repeated three times, unless when mentioned, and data were analyzed using Origin software (OriginLab Co., USA), in order to generate the *p*-values and all graphs. Results are shown as mean ± S.D, and statistical significance was analyzed by means of one-way ANOVA with Tukey's test for multiple comparison test using Origin software, and two-tailed Student's t test for single variable experiments using Microsoft Excel (Microsoft, USA).

Supporting Information

Supporting Information is available from the Wiley Online Library or from the author.

Acknowledgements

B.A.G.d.M., M.V.M., J.T.M., and M.A.P. contributed equally to this work. The authors thank Prof. Dr. Rodrigo Portes Ureshino, for his assistance with the use of the BSL-3 Lab and with virus acquisition, Prof. Dr. Alexandre Salgado Basso, for helpful discussion and for providing primers and reagents for flow cytometry analysis, Prof. José Luiz Proença Módena for kindly providing the SARS-CoV-2 strain used in the adaptation experiments, and Prof. Dr. Marcos Akira D'Ávila for the use of the rheometer. This work was supported by The São Paulo Research Foundation (FAPESP), grant numbers 2018/23039-3, 2018/12605-8, 2019/01255-9, 2021/03684-4, and 2020/05289-2; National Council for Scientific and Technological Development (CNPq), grant numbers 465656/2014-5, 309679/2018-4; and Coordination for the Improvement of Higher Education Personnel (CAPES), financial code 001.

Conflict of Interest

The authors declare no conflict of interest.

Data Availability Statement

The data that support the findings of this study are available from the corresponding author upon reasonable request.

Keywords

3D bioprinting, central nervous system, coronavirus, mouse-adapted, SARS-CoV-2

Received: January 6, 2022
Revised: April 5, 2022
Published online: May 6, 2022

[1] N. Chen, M. Zhou, X. Dong, J. Qu, F. Gong, Y. Han, Y. Qiu, J. Wang, Y. Liu, Y. Wei, J. '. Xia, T. Yu, X. Zhang, Li Zhang, *Lancet* **2020**, *395*, 507.
[2] A. A. Rabaan, S. H. Al-ahmed, R. Sah, A. Woodman, M. Al-Qahtani, S. Haque, H. Harapan, D. K. Bonilla-Aldana, P. Kumar, K. Dhama, A. J. Rodriguez-Morales, *Hum. Vaccines Immunother.* **2020**, *16*, 3011.
[3] World Health Organization, Coronavirus disease (COVID- 19) pandemic, https://covid19.who.int/ (accessed: April 2022).
[4] M. Hoffmann, H. Kleine-Weber, S. Schroeder, N. Krüger, T. Herrler, S. Erichsen, T. S. Schiergens, G. Herrler, N.-H. Wu, A. Nitsche, M. A. Müller, C. Drosten, S. Pöhlmann, *Cell* **2020**, *181*, 271.
[5] Y. Wang, S. Liu, H. Liu, W. Li, F. Lin, L. Jiang, Xi Li, P. Xu, L. Zhang, L. Zhao, Y. Cao, J. Kang, J. Yang, L. Li, X. Liu, Y. Li, R. Nie, J. Mu, F. Lu, S. Zhao, J. Lu, J. Zhao, *J. Hepatol.* **2020**, *73*, 807.
[6] X. Wang, Y. Zhou, N. Jiang, Q. Zhou, W-Li Ma, *Int. J. Infect. Dis.* **2020**, *95*, 433.
[7] J.-W. Li, T.-W. Han, M. Woodward, C. S. Anderson, H. Zhou, Y.-D. Chen, B. Neal, *Prog. Cardiovasc. Dis.* **2020**, *63*, 518.
[8] L. Pellegrini, A. Albecka, D L. Mallery, M J. Kellner, D. Paul, A P. Carter, L C. James, M A. Lancaster, *Cell Stem Cell* **2020**, *27*, 951.
[9] A. Varatharaj, N. Thomas, M. A. Ellul, N. W. S. Davies, T. A. Pollak, E. L. Tenorio, M. Sultan, A. Easton, G. Breen, M. Zandi, J. P. Coles, H. Manji, R. Al-Shahi Salman, D. K. Menon, T. R. Nicholson, L. A. Benjamin, A. Carson, C. Smith, M. R. Turner, T. Solomon, R. Kneen, S. L. Pett, I. Galea, R. H. Thomas, B. D. Michael, C. Allen, N. Archibald, J. Arkell, P. Arthur-Farraj, M. Baker, et al., *Lancet Psychiatry* **2020**, *7*, 875.
[10] C. K. Bullen, H. T. Hogberg, A. Bahadirli-Talbott, W. R. Bishai, T. Hartung, C. Keuthan, M. M. Looney, A. Pekosz, J. C. Romero, F. C. M. Sillé, P. Um, L. Smirnova, *ALTEX* **2020**, *37*, 665.
[11] A. Ramani, L. Müller, P. N. Ostermann, E. Gabriel, P. Abida-Islam, A. Müller-schiffmann, A. Mariappan, O. Goureau, H. Gruell, A. Walker, M. Andrée, S. Hauka, T. Houwaart, A. Dilthey, K. Wohlgemuth, H. Omran, F. Klein, D. Wieczorek, O. Adams, J. Timm, C. Korth, H. Schaal, J. Gopalakrishnan, *EMBO J.* **2020**, *39*, e106230.
[12] B.-Z. Zhang, H. Chu, S. Han, H. Shuai, J. Deng, Ye-F Hu, H.-R. Gong, A. C.-Y. Lee, Z. Zou, T. Yau, W. Wu, I. F.-N. Hung, J. F.-W. Chan, K.-Y. Yuen, J.-D. Huang, *Cell Res.* **2020**, *30*, 928.
[13] Lu Wang, D. Sievert, A E. Clark, S. Lee, H. Federman, B D. Gastfriend, E V. Shusta, S P. Palecek, A F. Carlin, J G. Gleeson, *Nat. Med.* **2021**, *27*, 1600.
[14] E. Song, C. Zhang, B. Israelow, A. Lu-Culligan, A. V. Prado, S. Skriabine, P. Lu, O-El Weizman, F. Liu, Y. Dai, K. Szigeti-Buck, Y. Yasumoto, G. Wang, C. Castaldi, J. Heltke, E. Ng, J. Wheeler, M. M. Alfajaro, E. Levavasseur, B. Fontes, N G. Ravindra, D. Van Dijk, S. Mane, M. Gunel, A. Ring, S A. J Kazmi, K. Zhang, C B. Wilen, T L. Horvath, I. Plu, et al., *J. Exp. Med.* **2021**, *218*, e20202135.
[15] F. Molina-Jimenez, I. Benedicto, V. L. Dao Thi, V. Gondar, D. Lavillette, J J. Marin, O. Briz, R. Moreno-Otero, R. Aldabe, T F. Baumert, F.-L. Cosset, M. Lopez-Cabrera, P L. Majano, *Virology* **2012**, *425*, 31.

[16] T. Hiller, J. Berg, L. Elomaa, V. Röhrs, I. Ullah, K. Schaar, A. C. Dietrich, M. A. Al-Zeer, A. Kurtz, A. C. Hocke, S. Hippenstiel, H. Fechner, M. Weinhart, J. Kurreck, *Int. J. Mol. Sci.* **2018**, *19*, 3129.
[17] J. Berg, T. Hiller, M S. Kissner, T H. Qazi, G N. Duda, A C. Hocke, S. Hippenstiel, L. Elomaa, M. Weinhart, C. Fahrenson, J. Kurreck, *Sci. Rep.* **2018**, *8*, 13877.
[18] S. Li, K. Yang, X. Chen, X. Zhu, H. Zhou, P. Li, Yu Chen, Y. Jiang, T. Li, X. Qin, H. Yang, C. Wu, B. Ji, F. You, Y. Liu, *Biofabrication* **2021**, *13*, 045013.
[19] C. F. Guimarães, L. Gasperini, A. P. Marques, R. L. Reis, *Nat. Rev.* **2020**, *5*, 351.
[20] C C. Bergmann, T E. Lane, S A. Stohlman, *Nat. Rev. Microbiol.* **2006**, *4*, 121.
[21] R. Chen, K. Wang, J. Yu, D. Howard, L. French, Z. Chen, C. Wen, Z. Xu, *Front. Neurol.* **2021**, *11*, 573095.
[22] S. J. Cleary, S. C. Pitchford, R. T. Amison, R. Carrington, C. L. R. Cabrera, M. Magnen, M. R. Looney, E. Gray, C. P. Page, *Br. J. Pharmacol.* **2020**, *177*, 4851.
[23] W. Li, C. Chen, A. Drelich, D. R. Martinez, L. E. Gralinski, Z. Sun, A. Schäfer, S. S. Kulkarni, X. Liu, S. R. Leist, D. V. Zhelev, L. Zhang, Y.-J. Kim, E. C. Peterson, A. Conard, J. W. Mellors, C.-T. Tseng, D. Falzarano, R S. Baric, D S. Dimitrov, *Proc. Natl. Acad. Sci. USA* **2020**, *117*, 29832.
[24] H. Gu, Q. Chen, G. Yang, L. He, H. Fan, Y.-Q. Deng, Y. Wang, Y. Teng, Z. Zhao, Y. Cui, Y. Li, X.-F. Li, J. Li, N.-N. Zhang, X. Yang, S. Chen, Y. Guo, G. Zhao, X. Wang, D.-Y. Luo, H. Wang, X. Yang, Y. Li, G. Han, Y. He, X. Zhou, S. Geng, X. Sheng, S. Jiang, S. Sun, et al., *Science* **2020**, *369*, 1603.
[25] R.-D. Jiang, M.-Q. Liu, Y. Chen, C. Shan, Y.-W. Zhou, X.-R. Shen, Q. Li, L. Zhang, Y. Zhu, H.-R. Si, Q. Wang, J. Min, X. Wang, W. Zhang, B. Li, H.-J. Zhang, R. S. Baric, P. Zhou, X.-L. Yang, Z.-L. Shi, *Cell* **2020**, *182*, 50.
[26] Y. Zhao, R L. Antoniou-Kourounioti, G. Calder, C. Dean, M. Howard, *Nature* **2020**, *583*, 825.
[27] S.-H. Sun, Q. Chen, H.-J. Gu, G. Yang, Y.-X. Wang, X.-Y. Huang, S.-S. Liu, N-N. Zhang, X.-F. Li, R. Xiong, Y. Guo, Y.-Q. Deng, W.-J. Huang, Q. Liu, Q.-M. Liu, Y.-L. Shen, Y. Zhou, X. Yang, T.-Y. Zhao, C.-F. Fan, Y.-S. Zhou, C.-F. Qin, Y.-C. Wang, *Cell Host Microbe* **2020**, *28*, 124.
[28] K. H. Dinnon III, S. R. Leist, A. Schäfer, C. E. Edwards, D. R. Martinez, S. A. Montgomery, A. West, B. L. Y. Jr., Y. J. Hou, L. E. Adams, K. L. Gully, A. J. Brown, E. Huang, M. D. Bryant, I. C. Choong, J. S. Glenn, L. E. Gralinski, T. P. Sheahan, R. S. Baric, *Nature* **2020**, *586*, 560.
[29] J. Wang, L. Shuai, C. Wang, R. Liu, X. He, X. Zhang, Z. Sun, D. Shan, J. Ge, X. Wang, R. Hua, G. Zhong, Z. Wen, Z. Bu, *Protein Cell* **2020**, *11*, 776.
[30] A. Muruato, M. N. Vu, B. A. Johnson, M. E. Davis-Gardner, A. Vanderheiden, K. Lokugamage, C. Schindewolf, P. A. Crocquet-Valdes, R. M. Langsjoen, J. A. Plante, K. S. Plante, S. C. Weaver, K. Debbink, A. L. Routh, D. Walker, M. S. Suthar, P.-Y. Shi, X. Xie, V. D. Menachery, *PLoS Biol.* **2021**, *19*, e3001284.
[31] J. Netland, D. K. Meyerholz, S. Moore, M. Cassell, S. Perlman, *J. Virol.* **2008**, *82*, 7264.
[32] P. B. Mccray, L. Pewe, C. Wohlford-Lenane, M. Hickey, L. Manzel, L. Shi, J. Netland, H. P. Jia, C. Halabi, C. D. Sigmund, D. K. Meyerholz, P. Kirby, D. C. Look, S. Perlman, *J. Virol.* **2007**, *81*, 813.
[33] E. S. Winkler, A. L. Bailey, N. M. Kafai, S. Nair, B. T. Mccune, J. Yu, J. M. Fox, R. E. Chen, J. T. Earnest, S. P. Keeler, J. H. Ritter, L.-I. Kang, S. Dort, A. Robichaud, R. Head, M. J. Holtzman, M. S. Diamond, *Nat. Immunol.* **2020**, *21*, 1327.
[34] G. A. Zornetzer, M. B. Frieman, E. Rosenzweig, M. J. Korth, C. Page, R. S. Baric, M. G. Katze, *J. Virol.* **2010**, *84*, 11297.
[35] X. Wang, Q. Ao, X. Tian, J. Fan, H. Tong, W. Hou, S. Bai, *Polymers* **2017**, *9*, 401.
[36] B. A. G. de Melo, Y. A. Jodat, S. Mehrotra, M. A. Calabrese, T. Kamperman, B. B. Mandal, M. H. A. Santana, E. Alsberg, J. Leijten, S. R. Shin, *Adv. Funct. Mater.* **2019**, *29*, 1906330.
[37] W J. Tyler, *Nat. Rev. Neurosci.* **2012**, *13*, 867.
[38] K. Saha, A J. Keung, E F. Irwin, Y. Li, L. Little, D V. Schaffer, K E. Healy, *Biophys. J.* **2008**, *95*, 4426.
[39] P. Moshayedi, G. Ng, J C. F. Kwok, G S. H. Yeo, C E. Bryant, J W. Fawcett, K. Franze, J. Guck, *Biomaterials* **2014**, *35*, 3919.
[40] M. Iwashita, H. Ohta, T. Fujisawa, M. Cho, M. Ikeya, S. Kidoaki, Y. Kosodo, *Sci. Rep.* **2018**, *9*, 3068.
[41] T. Distle, I. Lauria, R. Detsch, C. M. Sauter, F. Bendt, J. Kapr, S. Rütten, A. R. Boccaccini, E. Fritsche, *Biomedicines* **2021**, *9*, 261.
[42] B A. G. De Melo, Y A. Jodat, E M. Cruz, J C. Benincasa, SuR Shin, M A. Porcionatto, *Acta Biomater.* **2020**, *117*, 60.
[43] H. Duong, B. Wu, B. Tawil, *Tissue Eng., Part A* **2009**, *15*, 1865.
[44] N. Annabi, J. W. Nichol, X. Zhong, C. Ji, S. Koshy, A. Khademhosseini, F. Dehghani, *Tissue Eng., Part B* **2010**, *16*, 371.
[45] B A. G. de Melo, E M. Cruz, T N. Ribeiro, M V. Mundim, M A. Porcionatto, *J. Visualized Exp.* **2021**, *173*, e62691.
[46] C L. Lau, M. Kovacevic, T S. Tingleff, J S. Forsythe, H S. Cate, D. Merlo, C. Cederfur, F L. Maclean, C L. Parish, M K. Horne, D R. Nisbet, P M. Beart, *J. Neurochem.* **2014**, *130*, 215.
[47] S. Kyle, Z. M. Jessop, A. Al-Sabah, I. S. Whitaker, *Adv. Healthcare Mater.* **2017**, *6*, 1700264.
[48] K. Zhu, S. R. Shin, T. Van Kempen, Y.-C. Li, V. Ponraj, A. Nasajpour, S. Mandla, N. Hu, X. Liu, J. Leijten, Y.-D. Lin, M. A. Hussain, Y. S. Zhang, A. Tamayol, A. Khademhosseini, *Adv. Funct. Mater.* **2017**, *27*, 1605352.
[49] J. Shi, B. Wu, S. Li, J. Song, B. Song, W. F. Lu, *Biomed. Phys. Eng. Express* **2018**, *4*, 045028.
[50] J. Lu, Y. Fan, X. Gong, X. Zhou, C. Yi, Y. Zhang, J. Pan, *J. Cell. Physiol.* **2016**, *231*, 1752.
[51] B. Zhou, Y.-X. Zuo, R.-T. Jiang, *CNS Neurosci. Ther.* **2019**, *25*, 665.
[52] C. Escartin, E. Galea, A. Lakatos, J. P. O'callaghan, G. C. Petzold, A. Serrano-Pozo, C. Steinhäuser, A. Volterra, G. Carmignoto, A. Agarwal, N. J. Allen, A. Araque, L. Barbeito, A. Barzilai, D. E. Bergles, G. Bonvento, A. M. Butt, W.-T. Chen, M. Cohen-Salmon, C. Cunningham, B. Deneen, B. De Strooper, B. Díaz-Castro, C. Farina, M. Freeman, V. Gallo, J. E. Goldman, S. A. Goldman, M. Götz, A. Gutiérrez, et al., *Nat. Neurosci.* **2021**, *24*, 312.
[53] L. B. Haim, D H. Rowitch, *Nat. Rev. Neurosci.* **2017**, *18*, 31.
[54] P. P. Garcez, E. C. Loiola, R. Madeiro Da Costa, L M. Higa, P. Trindade, R. Delvecchio, J. M. Nascimento, R. Brindeiro, A. Tanuri, S. K. Rehen, *Science* **2016**, *352*, 816.
[55] P. P. Garcez, J. M. Nascimento, J. M. De Vasconcelos, R. Madeiro Da Costa, R. Delvecchio, P. Trindade, E. C. Loiola, L. M. Higa, J. S. Cassoli, G. Vitória, P. C. Sequeira, J. Sochacki, R. S. Aguiar, H. T. Fuzii, A. M. B De Filippis, J. L. Da Silva Gonçalves Vianez Júnior, A. Tanuri, D. Martins-De-Souza, S. K. Rehen, *Sci. Rep.* **2017**, *7*, 40780.
[56] M. Li, L. Li, Y. Zhang, X. S. Wang, *Infect. Dis. Poverty* **2020**, *9*, 1.
[57] M R. Alexander, C T. Schoeder, J A. Brown, C D. Smart, C. Moth, J P. Wikswo, J A. Capra, J. Meiler, W. Chen, M S. Madhur, *FASEB J.* **2020**, *34*, 15946.
[58] A. Maiese, A. C. Manetti, C. Bosetti, F. Del Duca, R. La Russa, P. Frati, M. Di Paolo, E. Turillazzi, V. Fineschi, *Brain Pathol.* **2021**, *31*, e13013.
[59] A. Maury, A. Lyoubi, N. Peiffer-Smadja, T. De Broucker, E. Meppiel, *Rev. Neurol.* **2020**, *177*, 51.
[60] S. Spudich, A. Nath, *Science* **2022**, *375*, 267.
[61] M. Marshall, *Nature* **2021**, *595*, 484.
[62] W. T. Harvey, A. M. Carabelli, B. Jackson, R. K. Gupta, E. C. Thomson, E. M. Harrison, C. Ludden, R. Reeve, A. Rambaut, S. J. Peacock, D. L. Robertson, *Nat. Rev. Microbiol.* **2021**, *19*, 409.

[63] S. Torices, R. Cabrera, M. Stangis, O. Naranjo, N. Fattakhov, T. Teglas, D. Adesse, M. Toborek, *J. Neuroinflammation* **2021**, *18*, 167.
[64] F. Jacob, S. R. Pather, W.-K. Huang, F. Zhang, S. Z. H. Wong, H. Zhou, B. Cubitt, W. Fan, C Z. Chen, M. Xu, M. Pradhan, D. Y. Zhang, W. Zheng, A. G. Bang, H. Song, J. Carlos De La Torre, G.-L. Ming, *Cell Stem Cell* **2020**, *27*, 937.
[65] G. M. Olivarria, Y. Cheng, S. Furman, C. Pachow, L. A. Hohsfield, S.-G. Charlene, R. Miramontes, J. Wu, M. S. Burns, K. I. Tsourmas, J. Stocksdale, C. Manlapaz, W. H. Yong, J. Teijaro, R. Edwards, K. N. Green, L. M. Thompson, T. E. Lane, *J. Virol.* **2022**, *96*, e01969-21.
[66] C. Ma, C. Gong, *J. Med. Virol.* **2020**, *93*, 4469.
[67] D. H. Brann, S. Adv, D. H. Brann, T. Tsukahara, C. Weinreb, M. Lipovsek, K. Van Den Berge, *Sci. Adv.* **2020**, *6*, eabc5801.
[68] K. Bilinska, P. Jakubowska, C. S. Von Bartheld, R. Butowt, *ACS Chem. Neurosci.* **2020**, *11*, 1555.
[69] V. S. Hernández, M. A. Zetter, E. C. Guerra, I. Hernández-Araiza, N. Karuzin, O. R. Hernández-Pérez, L. E. Eiden, L. Zhang, *Exp. Neurol.* **2021**, *345*, 113837.
[70] L. Cantuti-Castelvetri, R. Ojha, L D. Pedro, M. Djannatian, J. Franz, S. Kuivanen, F. Van Der Meer, K. Kallio, T. Kaya, M. Anastasina, T. Smura, L. Levanov, L. Szirovicza, A. Tobi, H. Kallio-Kokko, P. Österlund, M. Joensuu, F A. Meunier, S J. Butcher, M. S. Winkler, B. Mollenhauer, A. Helenius, O. Gokce, T. Teesalu, J. Hepojoki, O. Vapalahti, C. Stadelmann, G. Balistreri, M. Simons, *Science* **2020**, *860*, 856.
[71] J. Davies, H. S. Randeva, K. Chatha, M. Hall, D. A. Spandidos, E. Karteris, I. Kyrou, *Mol. Med. Rep.* **2020**, *22*, 4221.
[72] L. Bauer, B. Lendemeijer, L. Leijten, C. W. E. Embregts, B. Rockx, S. A. Kushner, F. M. S. de Vrij, D. van Riel, *Am. Soc. Microbiol.* **2021**, *6*, e00270.
[73] Y. Wang, Y. Cao, A. K. Mangalam, Y. Guo, R. G. LaFrance-Corey, J. D. Gamez, P. A. Atanga, B. D. Clarkson, Y. Zhang, E. Wang, R. S. Angom, K. Dutta, B. Ji, I. Pirko, C. F. Lucchinetti, C. L. Howe, D. Mukhopadhyay, *J. Cell Sci.* **2016**, *129*, 3911.
[74] X. Ou, Y. Liu, X. Lei, P. Li, D. Mi, L. Ren, L. Guo, R. Guo, T. Chen, J. Hu, Z. Xiang, Z. Mu, X. Chen, J. Chen, K. Hu, Q. Jin, J. Wang, Z. Qian, *Nat. Commun.* **2020**, *11*, 1620.
[75] J. Buchrieser, J. Dufloo, M. Hubert, B. Monel, D. Planas, M. M. Rajah, C. Planchais, F. Porrot, F. Guivel-Benhassine, S. Van Der Werf, N. Casartelli, H. Mouquet, T. Bruel, O. Schwartz, *EMBO J.* **2020**, *39*, e106267.
[76] J E. Carpenter, A C. Clayton, K C. Halling, D J. Bonthius, E M. Buckingham, W. Jackson, S M. Dotzler, J. P Card, L W. Enquist, C. Grose, *J. Virol.* **2016**, *90*, 379.
[77] V. Murta, A. Villarreal, A. J. Ramos, *Am. Soc. Neurochem.* **2020**, *12*, 1.
[78] S. Nampoothiri, F. Sauve, G. Ternier, D. Fernandois, C. Coelho, M. Imbernon, E. Deligia, R. Perbet, V. Florent, M. Baroncini, F. Pasquier, F. Trottein, C.-A. Maurage, V. Mattot, P. Giacobini, S. Rasika, *bioRxiv* **2020**.
[79] P. Tavčar, M. Potokar, M. Kolenc, M. Korva, T. Avšič-Županc, R. Zorec, J. Jorgačevski, *Front. Cell. Neurosci.* **2021**, *15*, 662578.
[80] G. Vargas, L. H. Medeiros Geraldo, N. Gedeão Salomão, M. Viana Paes, F. Regina Souza Lima, F. Carvalho Alcantara Gomes, *Brain, Behav. Immun.: Health* **2020**, *7*, 100127.
[81] F. Crunfli, V. C. Carregari, F. P. Veras, P. H. Vendramini, A. G. F. Valença, A. S. L. M. Antunes, C. Brandão-Teles, G. da S. Zuccoli, G. Reis-de-Oliveira, L. C. Silva-Costa, M. Saia-Cereda, A. C. Codo, P. L. Parise, D. A. T. Teixeira, G. F. de Souza, S. P. Muraro, B. M. S. Melo, G. M. Almeida, E. M. S. Firmino, R. G. Ludwig, G. P. Ruiz, T. L. Knittel, G. G. Davanzo, J. A. Gerhardt, P. B. Rodrigues, J. Forato, M. R. Amorim, N. B. Silva, M. C. Martini, M. N. Benatti, et al., *medRxiv* **2020**, *16*, 2020.10.09.20207464.
[82] E. Lavi, L. Cong, *Exp. Mol. Pathol.* **2020**, *115*, 104474.
[83] D. L. Wheeler, A. Sariol, D. K. Meyerholz, S. Perlman, *J. Clin. Invest.* **2018**, *128*, 931.
[84] J. Xu, S. Zhong, J. Liu, L. Li, Y. Li, X. Wu, Z. Li, P. Deng, J. Zhang, N. Zhong, Y. Ding, Y. Jiang, *Clin. Infect. Dis.* **2005**, *41*, 1089.
[85] X. Li, Z. Zhang, W. Tan, X. Sun, H. Ma, *PLoS One* **2016**, *11*, e0163807.
[86] K M. Johnson, R. Milner, S J. Crocker, *Neurosci. Lett.* **2015**, 600, 104.
[87] J. Gordon, S. Amini, M. K. White, in *Methods in Molecular Biology* (Eds: S. Amini, M. White), Humana Press, Totowa, NJ **2013**, p. 1078.
[88] J N. Hanson Shepherd, S T. Parker, R F. Shepherd, M U. Gillette, J A. Lewis, R G. Nuzzo, *Adv. Funct. Mater.* **2011**, *21*, 47.
[89] L. Zhou, A. C. Wolfes, Y. Li, D. C. W. Chan, H. Ko, F. G. Szele, H. Bayley, *Adv. Mater.* **2020**, *2*, 2002183.
[90] C L. Mcmahon, H. Staples, M. Gazi, R. Carrion, J. Hsieh, *Stem Cell Rep.* **2021**, *16*, 1156.
[91] N. Kanberg, J. Simrén, A. Edén, L.-M. Andersson, S. Nilsson, N J. Ashton, P.-D. Sundvall, B. Nellgård, K. Blennow, H. Zetterberg, M. Gisslén, *EBioMedicine* **2021**, *70*, 103512.
[92] S. A. Yi, K. H. Nam, J. Yun, D. Gim, D. Joe, Y. H. Kim, H.-J. Kim, J.-W. Han, J. Lee, *Viruses* **2020**, *12*, 1004.
[93] A. Paniz-Mondolfi, C. Bryce, Z. Grimes, R E. Gordon, J. Reidy, J. Lednicky, E. M. Sordillo, M. Fowkes, *J. Med. Virol.* **2020**, *92*, 699.
[94] J. Meinhardt, J. Radke, C. Dittmayer, J. Franz, C. Thomas, R. Mothes, M. Laue, J. Schneider, S. Brünink, S. Greuel, M. Lehmann, O. Hassan, T. Aschman, E. Schumann, R. L. Chua, C. Conrad, R. Eils, W. Stenzel, M. Windgassen, L. Rößler, H.-H. Goebel, H. R. Gelderblom, H. Martin, A. Nitsche, W. J. Schulz-Schaeffer, S. Hakroush, M. S. Winkler, B. Tampe, F. Scheibe, P. Körtvélyessy, et al., *Nat. Neurosci.* **2021**, *24*, 168.
[95] M. Khan, S.-J. Yoo, M. Clijsters, W. Backaert, A. Vanstapel, K. Speleman, C. Lietaer, S. Choi, T D. Hether, L. Marcelis, A. Nam, L. Pan, J W. Reeves, P. Van Bulck, H. Zhou, M. Bourgeois, Y. Debaveye, P. De Munter, J. Gunst, M. Jorissen, K. Lagrou, N. Lorent, A. Neyrinck, M. Peetermans, D. R. Thal, C. Vandenbriele, J. Wauters, P. Mombaerts, L. Van Gerven, *Cell* **2021**, *184*, 5932.
[96] M. C. Morton, V. N. Neckles, D. M. Feliciano, in *Methods in Molecular Biology* (Eds: K. Turksen), Humana, New York, NY **2002**, p. 75.
[97] F. R. Cugola, I. R. Fernandes, F. B. Russo, B. C. Freitas, J. L. M. Dias, K. P. Guimarães, C. Benazzato, N. Almeida, G. C. Pignatari, S. Romero, C. M. Polonio, I. Cunha, C. L. Freitas, W. N. Brandão, C. Rossato, D. G. Andrade, D. D. P. Faria, A. T. Garcez, C. A. Buchpigel, C. T. Braconi, E. Mendes, A. A. Sall, P. M. d. A. Zanotto, J. P. S. Peron, A. R. Muotri, P. C. B. Beltrão-Braga, *Nature* **2016**, *534*, 267.
[98] V. M. Corman, O. Landt, M. Kaiser, R. Molenkamp, A. Meijer, DKw Chu, T. Bleicker, S. Brünink, J. Schneider, M. L. Schmidt, D. G. Mulders, B. L. Haagmans, B. Van Der Veer, S. Van Den Brink, L. Wijsman, G. Goderski, J.-L. Romette, J. Ellis, M. Zambon, M. Peiris, H. Goossens, C. Reusken, M. PG Koopmans, C. Drosten, *Eurosurveillance* **2020**, *25*, 2000045.
[99] T. D. Schmittgen, K. J. Livak, *Nat. Protoc.* **2008**, *3*, 1101.
[100] J. Hadfield, C. Megill, S. M. Bell, J. Huddleston, B. Potter, C. Callender, P. Sagulenko, T. Bedford, R. A. Neher, *Bioinformatics* **2018**, *34*, 4121.
[101] K. Katoh, *Nucleic Acids Res.* **2002**, *30*, 3059.
[102] L.-T. Nguyen, H A. Schmidt, A. Von Haeseler, B. Q. Minh, *Mol. Biol. Evol.* **2014**, *32*, 268.
[103] P. Sagulenko, V. Puller, R. A. Neher, *Virus Evol.* **2018**, *4*, vex042.